Tectonophysics 854 (2023) 229808

Contents lists available at ScienceDirect

Tectonophysics

journal homepage: www.elsevier.com/locate/tecto

Megathrust complexity and the up-dip extent of slip during the 2021 Chignik, Alaska Peninsula earthquake

Chengli Liu [a,*], Yefei Bai [b,c,**], Thorne Lay [d], Yashan Feng [a], Xiong Xiong [a]

[a] School of Geophysics and Geomatics, China University of Geosciences, Wuhan, Hubei 430074, China
[b] Ocean College, Zhejiang University, Zhoushan, Zhejiang 316021, China
[c] Hainan Institute, Zhejiang University, Sanya, Hainan 572024, China
[d] Department of Earth and Planetary Sciences, University of California Santa Cruz, Santa Cruz, CA 95064, USA

ARTICLE INFO

Keywords:
2021 Chignik earthquake
Finite-fault inversion
Semidi segment
Tsunami simulation
Megathrust complexity
Up-dip limits of coseismic rupture

ABSTRACT

The up-dip extent of slip during large megathrust earthquakes is important for both tsunami excitation and subsequent tsunami earthquake potential, but it is unclear whether frictional properties and/or fault structure determine the up-dip limit. A finite-fault slip model for the 2021 M_W 8.2 Chignik, Alaska Peninsula earthquake obtained by joint inversion of seismic-geodetic data with model spatial extent constraints from the tsunami waves provides unusually good constraints on the up-dip edge of coseismic slip. Rupture initiated ~35 km deep and propagated unilaterally northeastward with large-slip (up to 8.4 m) distributed over a depth range of 26 to 42 km beneath the continental shelf. Aftershocks concentrate up-dip of the coseismic slip around a strong megathrust reflector with high Coulomb stress change. The ~25 km deep up-dip edge of slip strongly correlates with a change in plate interface reflectivity apparent in reflection profiles, indicating that a structural and frictional transition provided a barrier to shallower rupture.

1. Introduction

Accurate determination of the up-dip edge of coseismic slip during great megathrust earthquakes is a long-standing challenge of central importance to understanding tsunami generation by the event, along-dip dynamic rupture processes and changes in frictional properties, and potential for subsequent tsunami earthquakes (e.g., Lay et al., 2012; Sallarés and Ranero, 2019; Lay et al., 2019; Wirp et al., 2021; Yin and Denolle, 2021; Cheung et al., 2022). While finite-fault slip models are now routinely determined for large earthquakes (e.g., Ye et al., 2016; Hayes, 2017), resolution of the up-dip edge of slip remains very limited when using only global seismic and on-land geodetic data. Resolution of the seaward extent of coseismic rupture has improved for some recent great earthquakes by the inclusion of offshore geodetic data (e.g., Sato et al., 2011; Kido et al., 2011; Iinuma et al., 2012; Lay, 2018), repeat bathymetric imaging (e.g., Fujiwara et al., 2017; Tomito et al., 2017; Maksymowicz et al., 2017), and/or tsunami observations in finite-fault modeling (e.g., Yue et al., 2014; Heidarzadeh et al., 2016; Yamazaki et al., 2017; Romano et al., 2020), but only a few great events have well-resolved constraints on their up-dip slip extent.

The Alaska–Aleutian subduction zone involves convergence between the Pacific and North American plates at a rate of 5.1 to 7.5 cm/yr (DeMets et al., 2010), and many great earthquakes have occurred there over the last century (Sykes, 1971; Davies et al., 1981). Characteristics of large earthquakes and associated tsunamis along Alaska, the Alaska Peninsula, and the Aleutians vary significantly. The great 1964 M_W 9.2 Prince William and 1946 M_W 8.6 Aleutian earthquakes generated trans-Pacific tsunamis (Johnson and Satake, 1997; Tanioka and Seno, 2001; Ichinose et al., 2007). The down-dip eastern portion of the Shumagin segment (Fig. 1a) ruptured in 2020 in a major M_W 7.8 earthquake that generated a small tsunami (Crowell and Melgar, 2020; Liu et al., 2020; Ye et al., 2021; Xiao et al., 2021; Mulia et al., 2022a; Zhao et al., 2022; Bai et al., 2022). The Semidi segment located between the Shumagin and Kodiak segments (Fig. 1a) ruptured in the 1938 M_W 8.3 earthquake (Estabrook et al., 1994), also generating a relatively small tsunami (Johnson and Satake, 1994; Freymueller et al., 2021). Geodetic investigations indicated that the Semidi segment had accumulated a substantial slip deficit prior to 2021, exceeding that in the Shumagin segment, with some models indicating that strong geodetic locking extends all the way to the trench (e.g., Fournier and Freymueller, 2007; Li

* Corresponding author.
** Corresponding author at: Ocean College, Zhejiang University, Zhoushan, Zhejiang 316021, China.
E-mail addresses: liuchengli@cug.edu.cn (C. Liu), yfbai@zju.edu.cn (Y. Bai).

https://doi.org/10.1016/j.tecto.2023.229808
Received 17 September 2022; Received in revised form 25 February 2023; Accepted 5 March 2023
Available online 23 March 2023

and Freymueller, 2018; Drooff and Freymueller, 2021) (Fig. 1a). However, it has been demonstrated that the geodetic data have a very limited resolution of any slip deficit below the continental slope (Xiao et al., 2021; Zhao et al., 2022).

On July 29, 2021, the M_W 8.2 Chignik, Alaska Peninsula earthquake ruptured within the aftershock zone of the 1938 event. The coseismic slip pattern for the Chignik earthquake has been estimated in several studies (United States Geological Survey National Earthquake Information Center, 2021; Liu et al., 2022; Elliott et al., 2022; Mulia et al., 2022b; Ye et al., 2022). Most analyses indicate a strongly asymmetric bilateral rupture, with slip primarily extending toward the northeast. Liu et al. (2022) obtained a slip model by inverting extensive teleseismic and regional seismological and GNSS observations, finding that rupture expanded ~175 km along strike across depths from 17 to 43 km, with up to 8.6 m slip near the hypocenter. Elliott et al. (2022) inverted static GNSS displacements, high-rate GNSS waveforms, teleseismic waveforms, and InSAR displacements, finding coseismic slip extending from 9 to 37 km, with a peak slip of 6 m near the hypocenter. Their model is similar to that found using similar seismic and geodetic data sets by the U.S. Geological Survey National Earthquake Information Center (USGS-NEIC) in having slip extend to shallow depth (< 10 km). Mulia et al. (2022a, 2022b) determined a rupture model using joint analysis of tsunami waveforms and geodetic coseismic displacements, finding most slip located in the depth range from 22 to 39 km, and peak slip of 4.8 m at a depth of ~30 km. Ye et al. (2022) also included tsunami modeling with seismic and geodetic inversion, finding an elongated large-slip

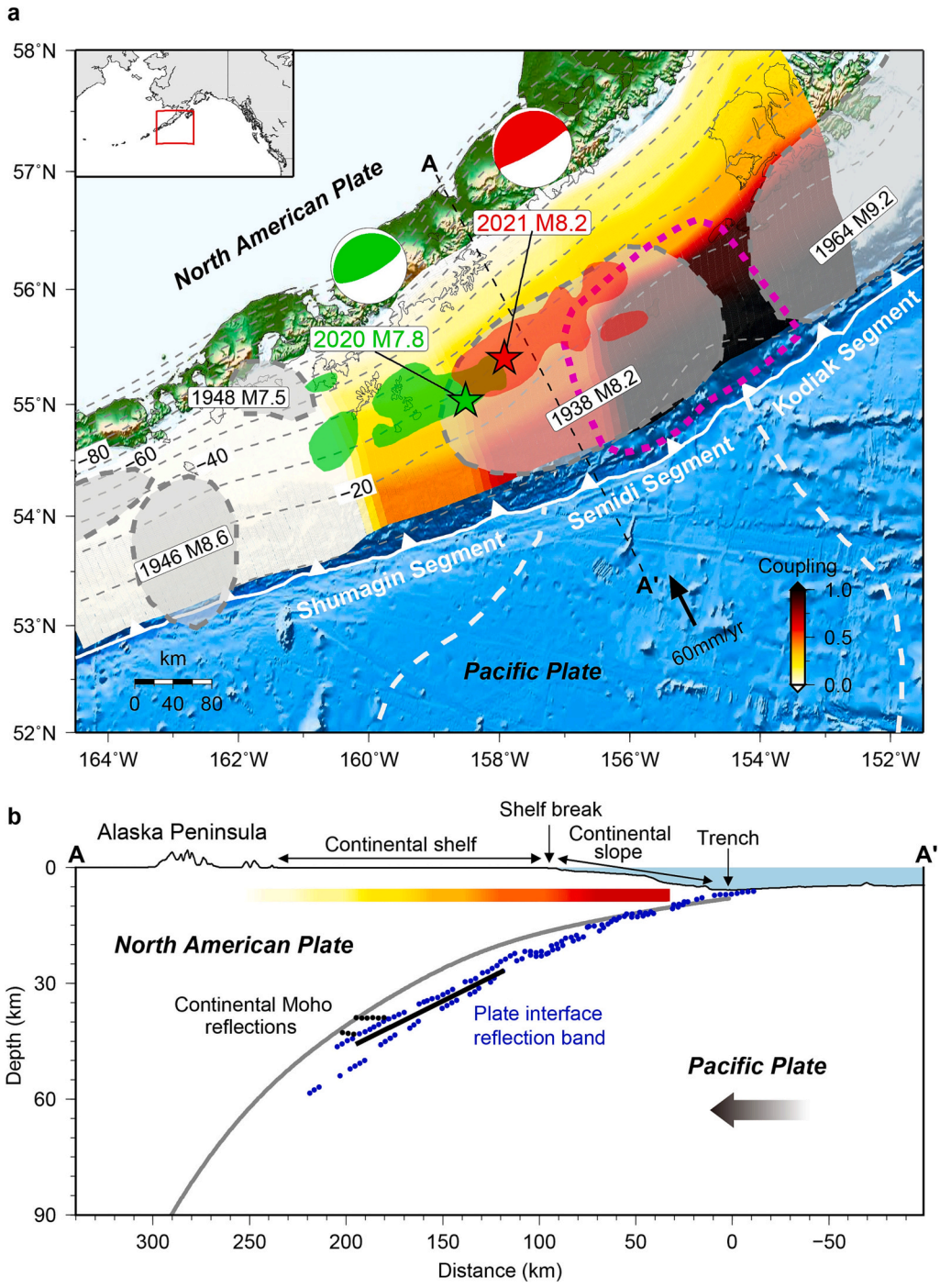

Fig. 1. Regional tectonic setting of the Alaska-Aleutian subduction zone and cross-section through the Semidi segment. a The gray shaded patches with dashed lines indicate the rupture regions of 1938, 1946, 1948, and 1964 events. The coseismic rupture areas of the 2020 *M*w7.8 Simeonof event and 2021 Mw 8.2 Chignik event are indicated with green-filled and red-filled patches, respectively. The thick magenta dashed line outlines the tsunami source model determined by Freymueller et al. (2021). The stars and focal mechanisms indicate the epicenters and GCMT solutions of the 2020 mainshock (green) and 2021 mainshock (red), respectively. Depths to the plate interface from Slab2 are shown by gray dashed lines with an interval of 10 km (Hayes et al., 2018). The plate coupling distribution is from Li and Freymueller (2018). The white barbed line shows the plate boundary between the Pacific plate and the North American plate, and the black arrow shows the relative motion between the Pacific plate and the North American plate (DeMets et al., 2010). White dashed lines outline the margins of the Zodiak Fan. The inset shows the general location of the study area. b Cross section indicating the fault model of the 2021 Chignik event and the geometry of the plate interface, and highlighting the broad flat continental shelf overlying the rupture zone, the shelf break, and the continental slope. Two blue dotted lines represent the thickness range of seismic reflection packages associated with the boundary zone of the plate interface. The black dotted lines show the extent of continental Moho. The thick gray curve is the slab interface profile from the Slab2 model along profile AA' in a. (For interpretation of the references to colour in this figure legend, the reader is referred to the web version of this article.)

distribution in the depth range of 30 to 40 km, with a small patch of large slip from 25 to 28 km in the northeast, and no slip shallower than 25 km. Some of these slip models were adjusted to fit the general strike and position of the slab interface in model Slab2 (Hayes et al., 2018), however, the Slab2 model has a 5–6 km shallower plate interface than that imaged in seismic reflection profiles in the Semidi segment (Kuehn, 2019) (Fig. 1b), so the absolute placement, as well as the estimated peak magnitude and up-dip extent of slip vary substantially among the published models.

The available finite-fault models for the 2021 Chignik earthquake are typical of large megathrust earthquake studies in that the up-dip limit of slip is very inconsistent between models, ranging from ~9 to ~30 km deep. This reflects the very limited resolution provided by distant geodetic observations on the Alaska Peninsula and by regional and teleseismic recordings. Even in the Shumagin segment, where offshore islands with geodetic instruments overlie the 2020 slip zone, the geodetic resolution of seaward prior slip deficit and coseismic slip below the continental slope is very limited (Xiao et al., 2021; Mulia et al., 2022a; Zhao et al., 2022). The upper plate in the Semidi segment has a broad continental shelf at shallow depth that extends over the large-slip zones of all of the 2021 Chignik slip models, with the shelf break located about 80–100 km from the trench (Fig. 1b). Recognizing the acute sensitivity of tsunami excitation to the absolute position of slip on the megathrust relative to the shelf break (e.g., Mulia et al., 2022b; Ye et al., 2022), in this study we seek to tighten the constraints on the up-dip edge of slip for the 2021 event. We first perturb a starting model (Liu et al., 2022) to fit the full suite of seismic, geodetic, and tsunami observations well, and then compare the results with the high-resolution imaging of the plate boundary interface to address controls on the up-dip limit of slip, along with considering aftershock distribution and Coulomb Failure Stress changes. The main contributions of this study are that the slip model is better spatially constrained than that in Liu et al. (2022), particularly for the up-dip extent of coseismic slip, and with improved confidence in the slip model, we can relate the bounds on slip distribution directly to reflection profiles along the megathrust and consider the important issue of whether the shallow megathrust has seismogenic potential.

2. Datasets and methodology

2.1. Data processing

We jointly analyze seismic, geodetic, and tsunami observations to resolve the rupture process of the 2021 Chignik earthquake. The observations for all near-field seismic and geodetic data sets are shown in Fig. S1. Data processing for the regional and teleseismic broadband, near-source strong-motion, and high-rate GNSS waveforms is the same as described in Liu et al. (2022), except that for the GNSS statics, we use revised solutions from the Geodesy Laboratory at Central Washington University (CWU).

2.2. Finite-fault inversion

As seismic and geodetic data can provide complementary constraints on the rupture process of large earthquakes, we used both data types to invert the rupture process of the 2021 Chignik event using a prescribed fault model. A nonlinear finite fault inversion method is employed (Ji et al., 2003) that simultaneously inverts geodetic and seismic observations. The simulated annealing algorithm solves for the slip magnitude and direction, rise time, and average rupture velocity for subfaults. For each parameter, we set specific search bounds and intervals. Here, the subfault size is chosen as 10 km × 10 km, and the slip on each subfault varies from 0.0 to 15 m. We allowed the rise and fall intervals of the asymmetric slip rate function for each subfault to vary from 1.0 to 10 s. Thus, the corresponding slip duration for each subfault is limited between 2 and 20 s. The rupture initiation time of each subfault changes within [L/v_ref-τ, L/v_ref + τ], L is the on-fault distance to the hypocenter, and v_ref is the average rupture velocity (Shao et al., 2011). v_ref and maximum perturbation time τ used during the final inversion are 2.5 km/s and 50 s, respectively. Green's functions for static displacements and seismic waveforms are computed using a 1-D layered velocity model (Niazi and Chun, 1989). Equal weighting among geodetic and seismic data sets was used in this study.

2.3. Tsunami modeling

We implement dispersive long wave model NEOWAVE (Non-hydrostatic Evolution of Ocean WAVE) to describe multiscale tsunami processes from the open ocean to the shore or vice versa (Yamazaki et al., 2011). NEOWAVE utilizes a vertical velocity term in the depth-integrated equations to account for weak dispersion comparable to low-order Boussinesq-type equations (Bai et al., 2018). The contribution from the vertical velocity term is essential in modeling of tsunami wave generation from kinematic seafloor deformation within a finite rise time and tsunami induced currents over steep continental slopes. The coupled wave-current dynamic processes are important for the resolution of developing tsunami waves in the near field and accurate reproduction of the DART and tide gauge records. The seafloor vertical displacement with respect to time is determined from rupture parameters of the finite-fault model using an elastic half-space solution (Okada, 1985), augmented by the horizontal motion of the seafloor slope (Tanioka and Satake, 1995). The numerical solution is obtained by the finite difference method with shock capturing scheme and nested computational grids in spherical coordinates. The grid nesting scheme allows two-way communications during the computation and provides multi-zoom capability to resolve wave amplitude and current with desirable resolution.

In modeling tsunamis generated from the finite-fault models, we apply two levels of grids to compute wave signals at Alitak, Sand Point, and King Cove in the Aleutian region and four levels of grids for Kahului and Hilo in the Hawaiian region as Fig. 3 shows. The level-1 grid extends across the North Pacific at 2-arcmin (~3700 m) resolution, which gives an adequate description of large-scale bathymetric features and optimal dispersion properties for modeling of trans-oceanic tsunami propagation with NEOWAVE (Li and Cheung, 2019). The level-2 grids resolve the continental shelf of the Alaska Peninsula at 30-arcsec (~925 m) and the insular shelves along the Hawaiian Islands at 24-arcsec (~740 m), which provides a transition to the level-3 grids for the Maui Nui and Big Island at 6-arcsec (~185 m) resolution. The finest grids at level-4 resolve the harbors and breakwaters where the tide gauges are located at 0.3-arcsec (9.25 m). A Manning number of 0.025 accounts for the subgrid roughness at the harbors. The digital elevation model includes General Bathymetric Chart of the Oceans (GEBCO) at 30-arcsec (~3700 m) resolution for the North Pacific, multibeam and laser imaging, detection, and ranging (LiDAR) data at 50 and ~ 3 m in the Hawaii region.

2.4. Coulomb failure stress

The Coulomb failure stress changes (ΔCFS) can be written as (Scholz, 2019).

$$\Delta CFS = \Delta\tau + \mu' \Delta\sigma_N$$

where $\Delta\tau$ and $\Delta\sigma_N$ are, respectively, changes in the shear stress and normal stress on a given fault (the receiver fault) caused by the source earthquake, and μ' is the apparent friction coefficient and set as 0.4. $\Delta\tau$ is positive in the slip direction of the receiver fault, and $\Delta\sigma_N$ is positive in the direction of normal stress that unclamps the receiver fault. Therefore, positive ΔCFS means the earthquake stress changes push the receiver fault closer to rupture, and vice versa (Freed, 2005). We computed the evolution of ΔCFS on the Slab2 (Hayes et al., 2018) geometry for the rupture models of the 2020 Shumagin earthquake (Bai

et al., 2022) and the 2021 Chignik earthquake (this study).

2.5. Thermal modeling

The first-order temperature distribution along the plate interface is computed using an analytical derivation of Molnar and England (1990). The temperature includes advective, radiogenic, and shear heating terms:

$$T = \frac{K_m}{SK_s}\frac{T_0 z}{\sqrt{\pi\kappa(t_0+t_s)}} + \frac{A_r z^2}{2SK_s} + \frac{\mu\rho g z(1-\lambda)Vz}{SK_s}$$

Here the S is a dimensionless parameter, which is defined as:

$$S = 1 + b\frac{K_m}{K_s}\sqrt{\frac{Vz\sin\delta}{\kappa}}$$

z is depth, t_s is the time to subduct to depth z, here, $t_s = z/V\sin\delta$, V is the average fault slip rate. See Table S1 for all parameter meanings and values used in the calculations.

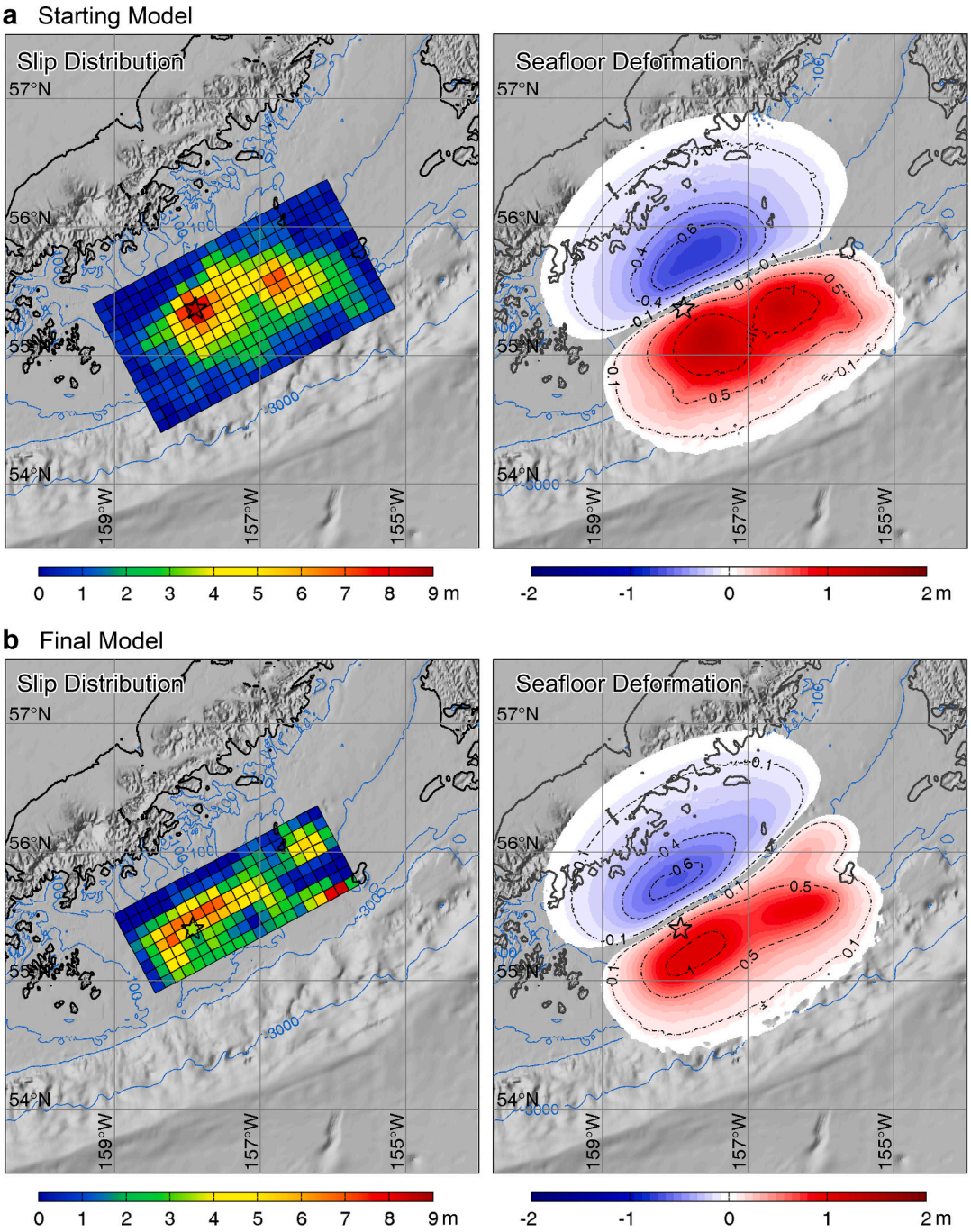

Fig. 2. Starting and final slip models for the 2021 Chignik, Alaska Peninsula earthquake. a Slip distribution (left) and vertical seafloor deformation (right) for the starting model from Liu et al. (2022). The star indicates the hypocenter from an initial USGS-NEIC location (55.325°N, 157.841°W, 32.2 km deep). b Slip distribution (left) and vertical sea floor deformation (right) for the final model, which fits all data well. Water depth contours of 100 m, 300 m, and 3000 m are shown by light blue dashed lines. The star indicates the updated USGS-NEIC hypocenter (55.364°N, 157.888°W, 35 km deep). (For interpretation of the references to colour in this figure legend, the reader is referred to the web version of this article.)

3. Results

3.1. Model configuration and inversion procedure

Using an iterative seismic+geodetic inversion and tsunami modeling procedure (Bai et al., 2022), we determine a finite-fault slip model that accounts for the complete set of seismic, geodetic, and tsunami observations for the 2021 Chignik earthquake. A planar fault model is assumed along with the updated USGS-NEIC hypocentral depth of 35 km (at 55.364°N, 157.888°W). The fault plane strike is 242°, and the dip is 14°, similar to the USGS-NEIC W-phase solution and the geometry of the interface as imaged by reflection seismology (Kuehn, 2019). Adopting the same extensive seismic and geodetic data sets used in Liu et al. (2022) (Fig. S1), we invert for a kinematic slip model, then predict tsunami signals using a non-hydrostatic code NEOWAVE in which the kinematic sea floor motion excites the tsunami (Yamazaki et al., 2011; Bai et al., 2014). The iterative seismic+geodetic inversion and tsunami modeling procedure basically involve initial inversion of the seismic and geodetic data, and then calculation of the tsunami predictions for that model. Misfits of the tsunami first-arrival timing and amplitudes prompt adjustments of the model parameterization (guided by extensive sensitivity tests), primarily involving reduction of the up-dip and/or along-strike extent of the model grid, and the procedure iterates. Examples of tests with gradually truncating up-dip grid extents are shown in Fig. S2. Essentially a zero-slip constraint is imposed on regions of the model grid to spatially constrain the subsequent inversion, systematically improving the fit to the tsunami data while still achieving a comparable fit to the seismo-geodetic data. This procedure works particularly well in this situation because even small amounts of slip too far seaward on the up-dip edge of the inversion can produce too early and too large of tsunami signals as shown in Bai et al. (2022) and Ye et al. (2022).

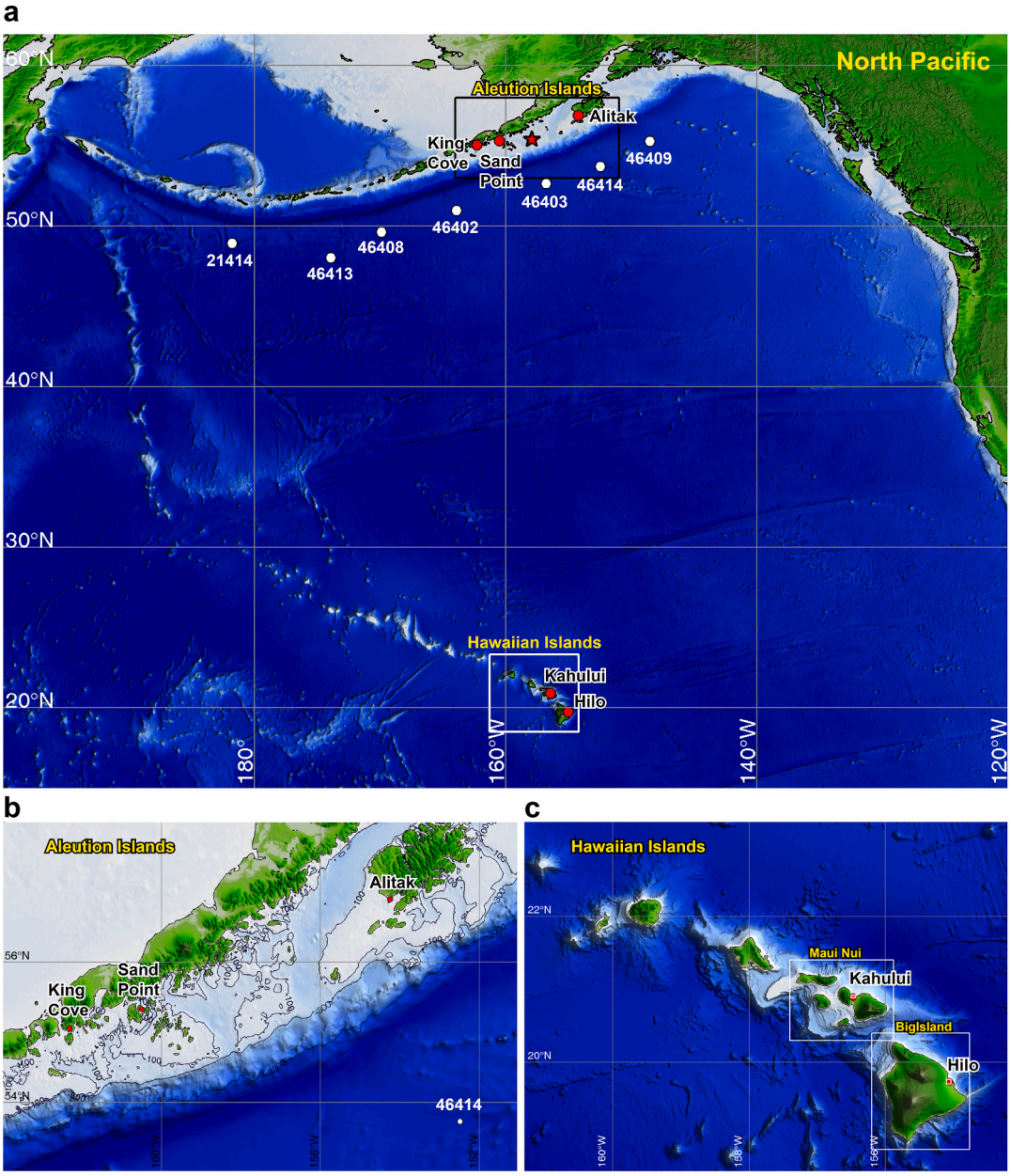

Fig. 3. Computational bathymetry and location maps of tide gauge and DARTs. a Level-1 grid with outlines of level-2 grids, DART locations (white circles), and Sand Point, King Cove, Alitak, Kahului, and Hilo tide gauges (red circles). b Level-2 grid for the source region. c Level-2 grid for the Hawaiian Islands with outlines of level-3 and 4 grids. (For interpretation of the references to colour in this figure legend, the reader is referred to the web version of this article.)

3.2. Tsunami simulation

Fig. 2a shows the starting slip model from Liu et al. (2022) and the corresponding static vertical deformation of the seafloor, while Fig. 2b shows the final model obtained in the iterative process, which has contracted model dimensions. The seafloor deformations, as shown in Fig. 2, drive the tsunami calculations using NEOWAVE. Fig. 3a shows the Level-1 bathymetric structure for the North Pacific with the locations of tide gauge and deep-water pressure sensors (DART stations) used in the modeling. Nested grids are used to incorporate Level-2 (Fig. 3b, c) to Level-3 (insets in Fig. 3c) up to Level-5 higher resolution grids around the source area and near the tide gauges. Fig. 4 compares observed tsunami signals with the predictions of the two models in Fig. 2. The starting model produces early predicted tsunami arrivals with too large amplitudes at the DART stations and in Hawaii (Fig. 4a). This is a consequence of having seafloor uplift on the continental slope (Fig. 2a), as even modest uplift under deep water excites larger amplitude, shorter period signals than does large seafloor deformation below the continental shelf (e.g., Mulia et al., 2022a, 2022b; Ye et al., 2022).

3.3. Optimized slip model parameters

The final slip model has rupture initiate at 35 km depth and propagate predominantly unilaterally, with three patches of large slip in the depth range of 26 to 42 km, along a total rupture length of 200 km, with a maximum slip of ~8.4 m (Fig. 5a). The total seismic moment is $M_0 = 2.44 \times 10^{21}$ Nm ($M_W = 8.2$), with the source duration being 110 s. The centroid location of the slip model is at 55.61°N, 157.45°W, 36.5 km

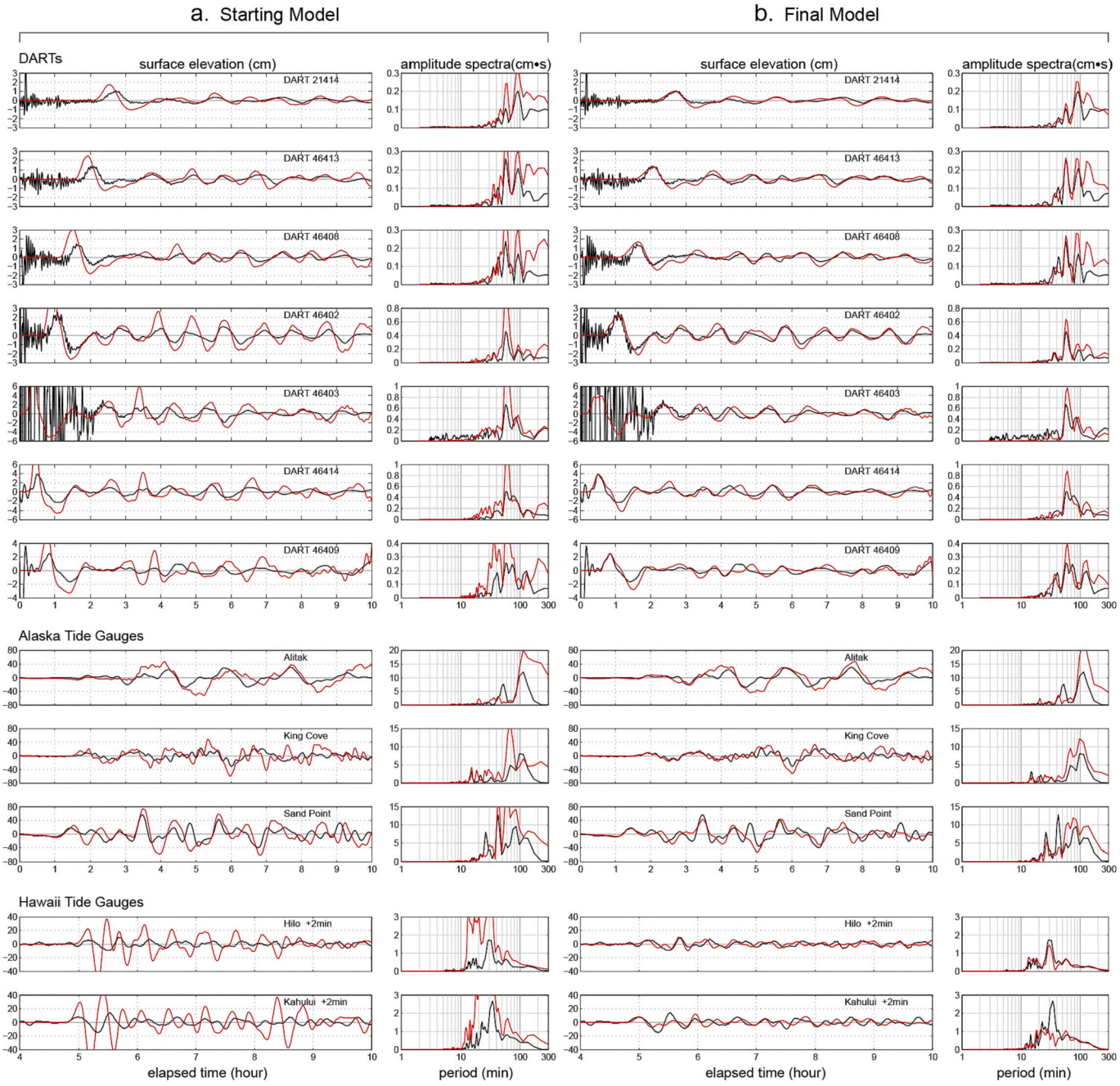

Fig. 4. Tsunami predictions at DARTs for the finite-fault slip models. a Comparison of tsunami waveforms at DARTs and Tide Gauges for the starting model from Liu et al. (2022). b Comparison of tsunami waveforms for the final slip model.

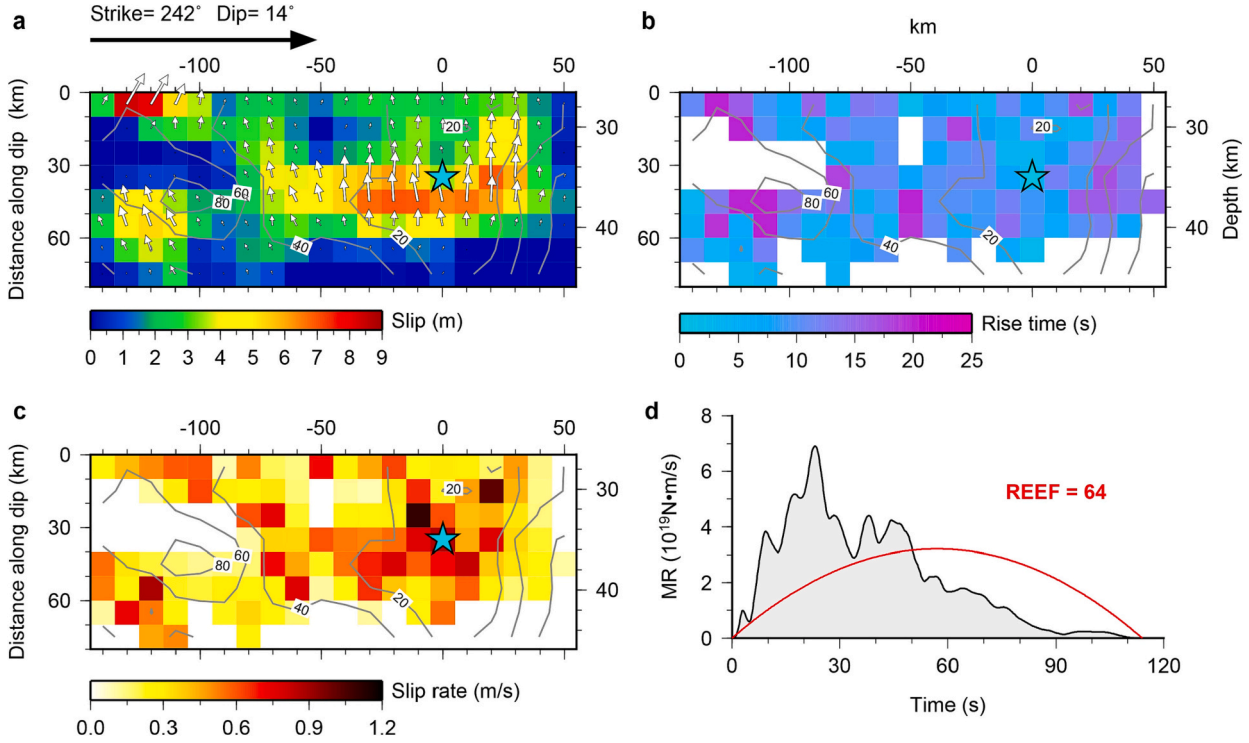

Fig. 5. Final slip model of the 29 July 2021 Chignik earthquake. a The slip model of the 2021 Chignik event. The slip amplitude is indicated by the colour bar. The cyan-filled star shows the hypocenter. Gray contours outline the rupture initiation time with an interval of 20 s. White arrows represent the rupture direction of the hanging wall. b The spatial distribution of rise time. Subfaults with slip <1.0 m are excluded, and colour shows the value of rise time. c The slip rate distribution, which is defined by the ratio of fault slip and rise time. d The moment-rate function (MRF) of the final slip model. The red line indicates the parabolic shape of the MRF for a minimum value of radiated energy based on the seismic moment and duration of the 2021 Chignik event. (For interpretation of the references to colour in this figure legend, the reader is referred to the web version of this article.)

deep, comparable with the USGS-NEIC *W*-phase centroid estimate (M_0 = 2.36 × 10^{21} N·m; 55.42°N, 157.91°W and 35.5 km deep), which ensures that our solution is compatible with very long-period seismic data. Subfaults with slip <1 m are excluded due to their low reliability, and the average rise time (Fig. 5b) and slip rate (Fig. 5c) of the included subfaults are 10 s and 0.4 m/s, respectively. There is an overall correlation between slip and slip rate, but locally this has scatter in areas of low total slip. The large slip patch at the shallow end of the rupture in the northeast appears to be for a relatively isolated asperity that was triggered. It has a moderate slip rate and long rise time, which accounts for the large slip. This feature of the model is controlled by the nearby displacement at GNSS station AC13 (Fig. 6) with the up-dip constraint from tsunami arrival times at DARTs 46,403 and 46,414 (Figs. 3a and 4a). Snapshots of the space-time slip evolution indicate that slip spread around the deep side of the hypocenter during the first 20 s with a higher slip rate (Fig. S3), then the rupture expanded asymmetrically to the northeast, with a general increase in rise time. Most of the seismic moment was released within 90 s (Fig. 5d), and the overall average rupture velocity is ~2.5 km/s.

Waveform fits for the model in Fig. 5a for multiple data sets are shown in Figs. 4b and 6 (all additional data comparisons are shown in Figs. S4-S6). The final slip model accounts well for all observations, fitting the geodetic and seismic data comparably well to the starting model (Liu et al., 2022) while notably improving the fit to the tsunami signals (Fig. 4b). The distribution of the regional data sets provides good constraints on the down-dip edge of slip and the along-strike extent of the rupture. A few notable misfits for late high frequency arrivals are apparent in some regional waveforms, such as stations CHN and S19K, likely due to unmodeled site effects and oversimplification by the use of a 1D velocity model. Fits to the vertical displacements at a few nearby GNSS stations, such as AC21 and AC13 are not quite as good as in the starting model, but these are very sensitive to changes in along-strike length of the model, which was reduced in fitting the tsunami (Fig. 2). By constraining the model dimensions in the up-dip (seaward direction), we preclude any uplift beyond the shelf break, and together with minor along-strike contraction, the final model fits the arrival times and amplitudes of the tsunami observations well (Fig. 4b). The dramatic difference in tsunami excitation across the north Pacific for the starting and final models is shown in Fig. 7.

Essentially, the seaward extent of significant slip (>0.5–1 m) is bounded to depths >25 km in order to predict the tsunami signals acceptably. The horizontal resolution of the up-dip edge of >1 m coseismic slip is about ±10 km, which is a remarkably tight resolution for a great earthquake finite-fault model. Mulia et al. (2022b) show that the USGS model overpredicts the tsunami amplitudes, and in Fig. S7, we show that the model of Elliott et al. (2022) does as well, confirming that having any significant slip shallower than ~25 km violates the tsunami observations in the same way as the starting model here (Fig. 4a). The model of Ye et al. (2022) is similar to our final model in having no slip shallower than 25 km and fits the tsunami data well, but we fit many more regional broadband and strong-motion signals, along with high-rate GNSS time series, providing excellent resolution of the slip, as confirmed by checkerboard tests (Fig. S8). Overall, the good fits between the extensive observations and synthetics indicate the reliability of our coseismic slip model for the 2021 Chignik earthquake in Fig. 5.

3.4. Stress changes

We computed the static stress drop distribution for our model (Fig. S9) using the method proposed by Ripperger and Mai (2004). The static stress change varies approximately from 16 MPa (stress drop) to −8 MPa (stress increase) over the fault plane. The static stress drop is predominantly contributed by thrust motion. Stress change resolved for along-strike motion is between 2.6 MPa and − 24 MPa, with a localized

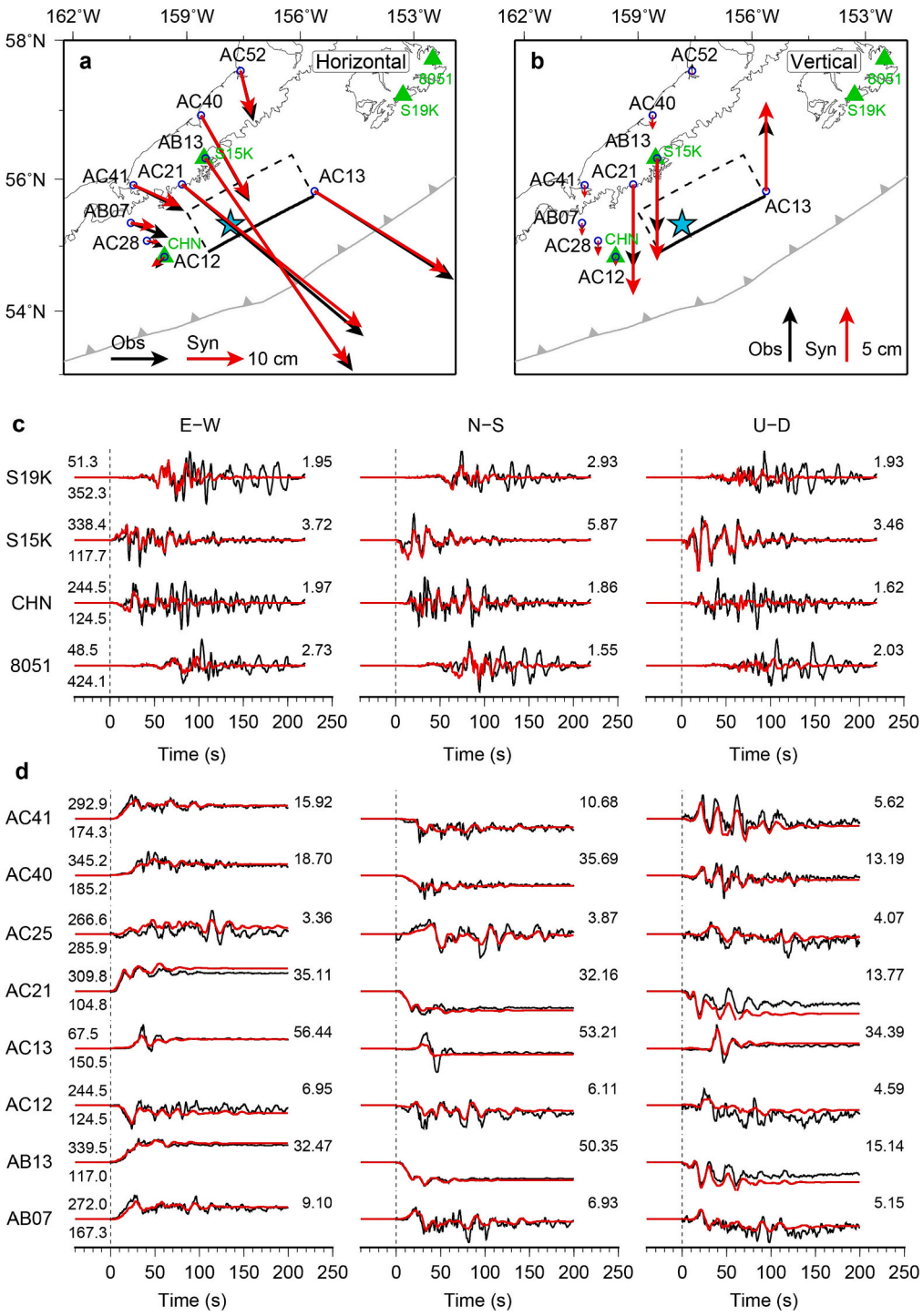

Fig. 6. Comparison of subsets of the observed data and synthetics for the final slip model. a and b show horizontal and vertical comparisons between observed (black) and computed (red) static GNSS displacements for the final slip model shown in Fig. 5a. c Observed (black lines) and predicted (red lines) waveform comparisons for three-component strong-motion ground velocities in cm/s. d Comparisons of subsets of high-rate GNSS displacement time series (black) and synthetic seismograms (red) in cm. Station names are indicated on the left, and peak values are shown on the upper right. The azimuth (above) in degrees and epicentral distance (below) in km are shown at the beginning of each waveform. All data comparisons are shown in Figs. S4-S6. (For interpretation of the references to colour in this figure legend, the reader is referred to the web version of this article.)

large stress increase in a shallow slip patch in the northeast of the model (Fig. 1a), in the vicinity of significant local postseismic slip (Fig. S1). The slip-weighted average stress drop is ~14 MPa, which is somewhat higher than average for a megathrust earthquake (Ye et al., 2016), but this may reflect the tighter than usual spatial resolution of the slip distribution. The broadband radiated energy estimated for the event is 3.1×10^{16} J over a 93 s rupture duration (IRIS radiated energy). Using the seismic moment from the finite fault inversion, we find a moment-scaled radiated energy of 1.3×10^{-5}, which is slightly above the average value of 1.06×10^{-5} for interplate thrusts (Ye et al., 2016). The moment-rate function (Fig. 5d) is relatively rough, and following Ye et al. (2018), the radiated energy enhancement (REEF) parameter is 64, which is moderately high, typical of relatively complex moment-rate function events.

The distribution of USGS-NEIC aftershocks in the first 3 months after the 2021 Chignik earthquake relative to the final slip model in Fig. 5a is shown in Fig. 8a. The location precision for the catalog locations is on the order of ±10 km due to the one-sided distribution of the regional stations. The precision of the up-dip limit of slip is on the same scale, due to the inclusion of the tsunami data (Fig. S2), so it is reasonable to compare the aftershock locations relative to the improved slip model. Most aftershock activity is concentrated on the margins of the large slip zone, especially along the up-dip edge of slip. The aftershock activity extends further seaward to near the shelf break than the early aftershock

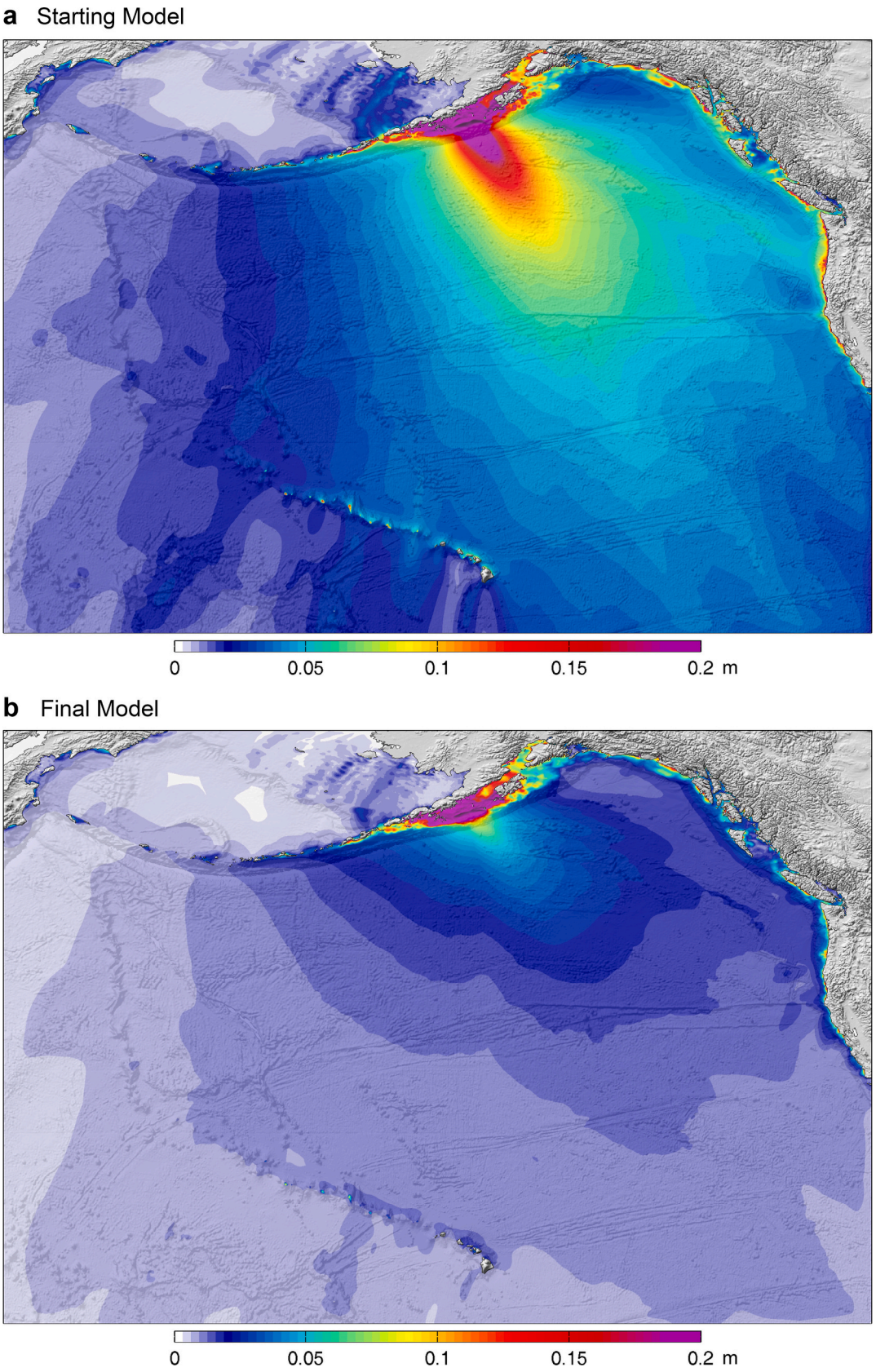

Fig. 7. Maximum sea surface elevation maps extending from the source region across the northern Pacific to Hawaii. a and b Sea surface elevation predicted from the finite-source model of Liu et al. (2022) and final slip model of the 2021 event, respectively.

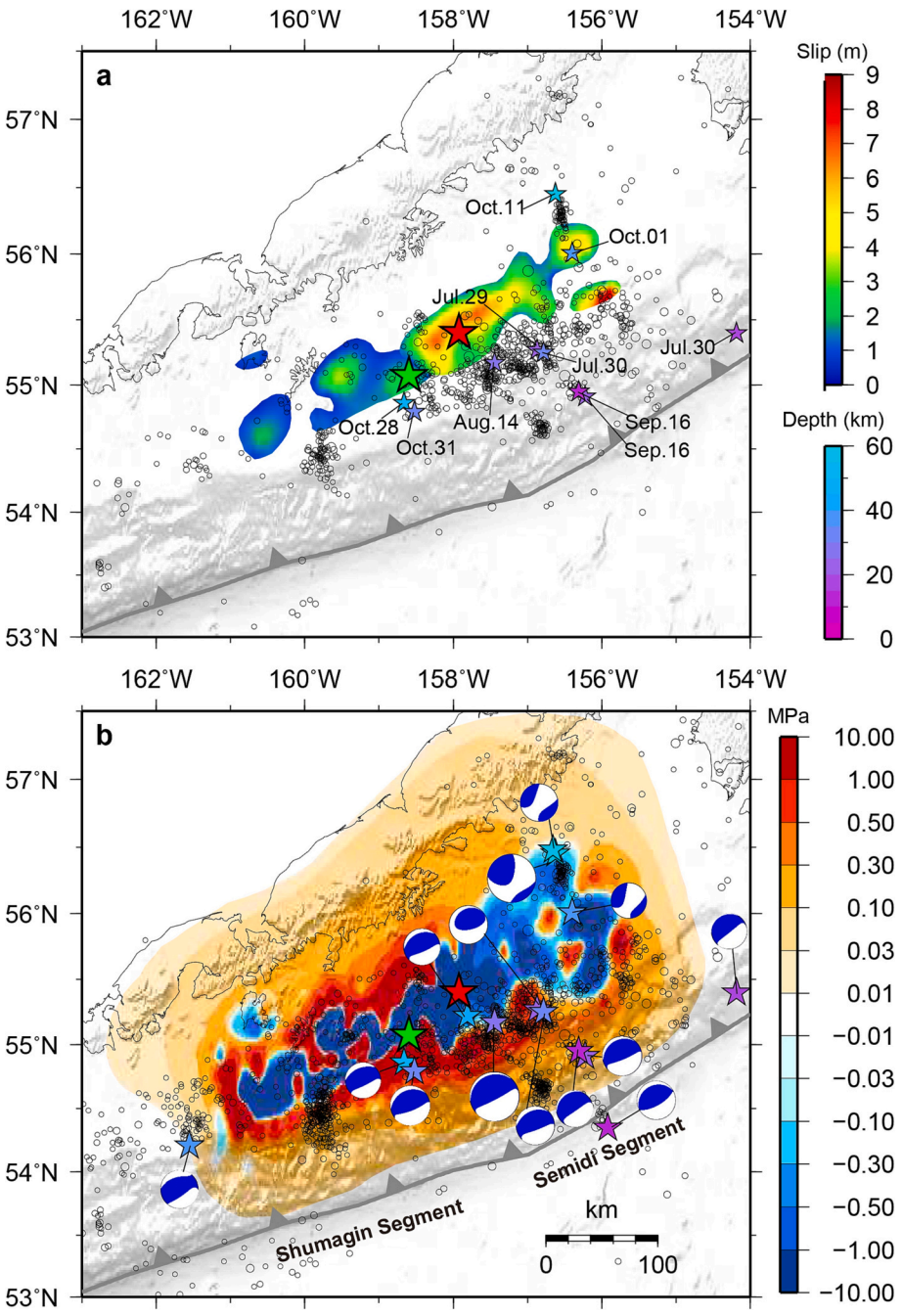

Fig. 8. Aftershocks distribution and Coulomb stress changes. a Superposition of first 3 months aftershocks (open circles for events with $M_W < 5$) with magnitude ≥2.5 from USGS-NEIC catalog on the final slip models of the 2020 and 2021 mainshocks. The green and red stars indicate the epicenter of the 2020 and 2021 events, respectively. Other colored stars indicate aftershocks with magnitude ≥5 at different depths. b Computed Coulomb stress changes on the Slab2 plate interface caused by the 2020 and 2021 events. Global centroid moment-tensor (GCMT) focal mechanisms with magnitude ≥5.0 one year after the 2021 earthquake are shown in blue. Open circles, scaled by magnitude, show one-year aftershocks of the 2021 event. (For interpretation of the references to colour in this figure legend, the reader is referred to the web version of this article.)

activity along the 2020 Simeonof earthquake rupture, which was mostly deeper than 25 km (Bai et al., 2022). The largest aftershock, on October 11, 2021, has M_W 6.9 and ruptured within the Pacific plate northeast and down-dip of the slip zone. Focal mechanism solutions for 5 events shallower than the up-dip edge all have thrust-faulting geometries, with the largest event being an M_W 7.0 thrust event on August 14, 2021 with a centroid at 55.17°N, −157.45°W, 25 km deep. Only two of the events locate further seaward on September 16, 2021 with M_W 5.6 and 5.3 and centroid depths of 21.4 and 12.0 km, respectively (Fig. 8a). There are several localized clusters of shallow activity and very sparse activity in the shallow megathrust <20 km deep below the continental slope. The overlap of aftershocks and slip is reduced relative to the starting model (Liu et al., 2022) by virtue of the deeper up-dip edge of slip in the final model.

Coulomb failure stress changes were computed using the megathrust geometry as the target fault (Fig. 8b). Coulomb stress increased substantially up-dip of the slip, where most aftershocks occurred, and the Coulomb stress is also enhanced in the down-dip region, although aftershocks are few in number. The large aftershocks ($M \geq 5.0$) have thrust fault mechanisms, except for three normal-faulting events in the northeastern part of the rupture that occurred deeper within the subducting Pacific plate. In addition, it is worth noting that the up-dip megathrust of the eastern Shumagin segment has substantial stress increases exceeding 0.3 MPa, but the seismicity is pretty weak, leaving a substantial area of unknown frictional state.

4. Discussion

Similarly well-resolved slip distributions for the 2020 Simeonof M_W 7.8 (Bai et al., 2022) and 2021 Chignik M_W 8.2 earthquakes have been

determined by joint analysis of seismic, geodetic, and tsunami observations. In both cases, the resolution of the up-dip edge of slip exploits the acute tsunamigenic sensitivity to placement of slip along the megathrust relative to the shelf break; a relatively rare opportunity enabled by the broad shallow continental shelf in this region. The up-dip limit of slip in the two adjacent events is almost uniform, at about 25 km depth (Fig. 1a). This is much deeper than the typical up-dip aseismic megathrust region commonly associated with weak velocity strengthening materials and low effective stresses associated with elevated pore fluid pressure (Li et al., 2015). The seaward extent of most aftershock activity is limited to beneath the shelf for both events, noting that the largest aftershock of the 2020 event (M_W 7.6) on October 19, 2020 was a seaward intraplate rupture with many intraplate aftershocks (Fig. 8a). Aftershock activity does extend further seaward along the Chignik rupture zone and there are localized patches of aftershocks beneath the continental slope.

The similarity in the up-dip extent of the slip zones for the 2020 and 2021 events is surprising given the strong lateral gradient in geodetic coupling between the Shumagin and Semidi segments that preceded the events (Fig. 1a). Both events have abrupt termination in up-dip slip along a nearly continuous line (Fig. 1a), suggesting some common control on the coseismic sliding. Deep-sounding reflection profiles from the 2011 Alaska Langseth Experiment to Understand the megaThrust (ALEUT) project provide important information on the along-dip variation in seismic reflectivity (Kuehn, 2019; Li et al., 2015; Bécel et al., 2017; Li et al., 2018; Shillington et al., 2022). While imaging resolution is best in the frontal prism of the overriding plate, beneath the continental slope, the plate boundary fault is imaged as deep as 35 to 50 km in these profiles, spanning the rupture extent of the large events. Fig. 9 shows cross-sections along 4 of the ALEUT reflection profiles in the Semidi and Shumagin segments, with the position of the well-resolved fault models superimposed on the highlighted plate interface reflectors from Kuehn (2019) and Shillington et al. (2022).

The up-dip limit of slip for both events is close to along-dip transitions in reflectivity from a relatively irregular reflector with deformed metasediments in a low velocity zone 100–250 m thick in the upper 10 to 25 km of the sections to more planar quasi-parallel banded reflectors within a depth range of 2 to 5 km below 25 km (Kuehn, 2019; Li et al., 2015; Shillington et al., 2022). Of course, decreasing resolution with depth may obscure deeper roughness, but the images in shallower regions are assumed to be reliable (we simply reproduce the reflector interpretations shown in the cited papers). Some of the shallow roughness of the megathrust is likely associated with splaying thrust faults that intersect the plate boundary, while upper plate reflectors from the lower crust and continental Moho are distinct from the plate interface reflectors (Kuehn, 2019; Li et al., 2015). The continental Moho appears to intersect the plate interface at a depth of 30 to 45 km along the Semidi segment (Fig. 1b), and possibly shallower (22 to 33 km) along the

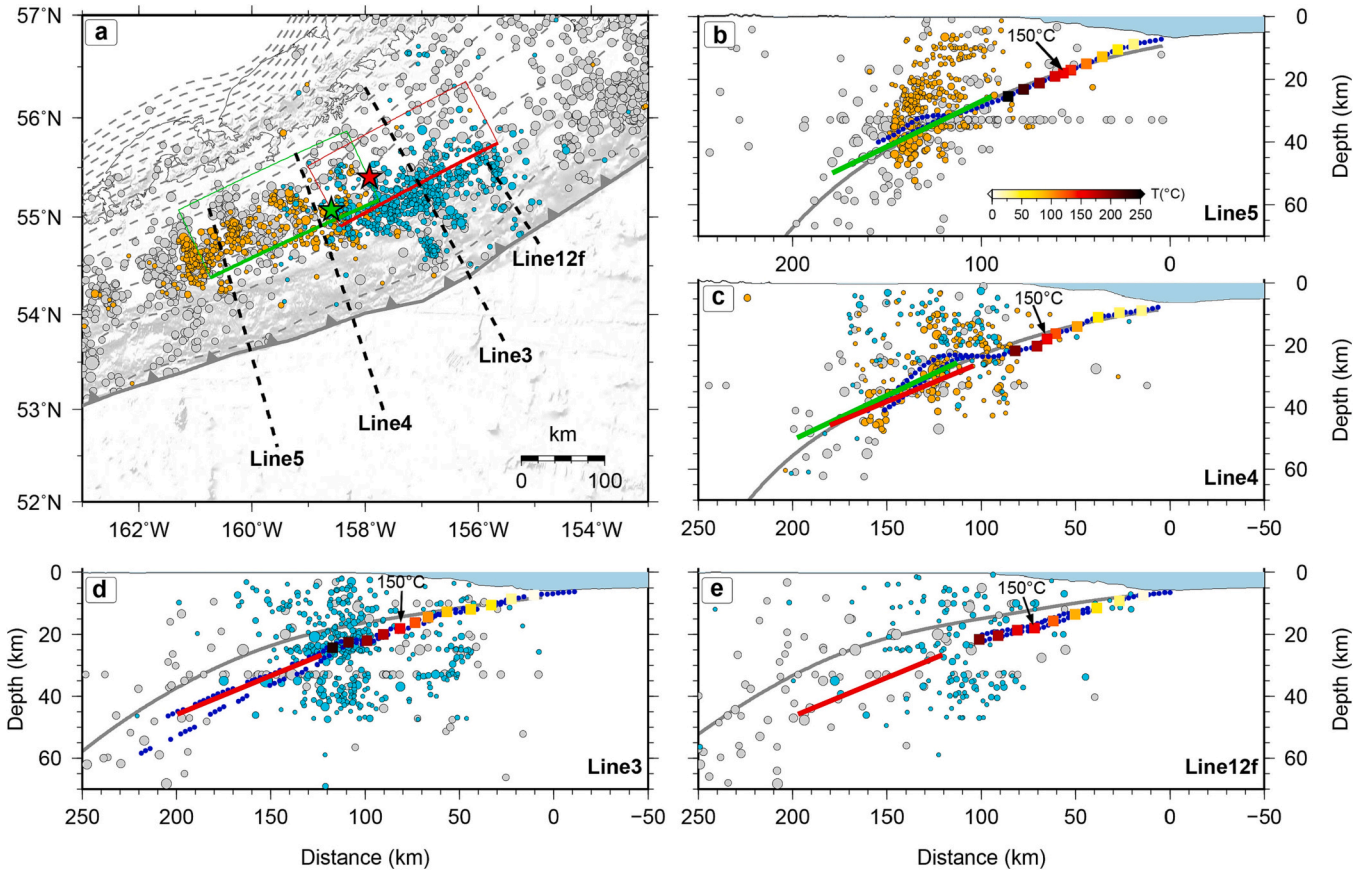

Fig. 9. Cross sections of fault model and seismic lines. a Spatial distribution of historical earthquakes (gray dots) and 2 months aftershocks of the 2020 Simeonof event (orange dots) and 2021 Chignik event (cyan dots). The green and red rectangles represent the fault model margins of these two events, with a solid line showing the shallow edge. Dashed contours indicate the plate interface position for model Slab2, with depth increments of 10 km. Black dashed lines indicate the locations of the seismic lines. b, c, d, and e are profiles along seismic lines 5 (Fig. 4. In Shillington et al., 2022), 4 (Fig. 4 in Shillington et al., 2022; Fig. 3.7.2 in Kuehn, 2019), 3 (Figs. 3.7.1, 4.6.1, 4.6.2 and 4.6.3 in Kuehn, 2019) and 12f (Fig. 3.8.2 in Kuehn, 2019), respectively. Gray curves represent the plate interface position for model Slab2. Temperatures on the plate interface are shown as colored squares according to the colour bar in b. Blue dots represent the original authors (Shillington et al., 2022; Kuehn, 2019) interpretation of the thickness extent of seismic reflection packages associated with the boundary zone of the plate interface. Green and red solid lines in the profiles indicate the model location of the 2020 event (Bai et al., 2022) and 2021 event (this study), respectively. (For interpretation of the references to colour in this figure legend, the reader is referred to the web version of this article.)

Shumagin segment, although a thicker continent has not been ruled out (Li et al., 2015; Shillington et al., 2022). If this is the true continental Moho depth, the primary coseismic rupture zones may lie along the mantle of the upper plate. The change in the overriding plate at the Moho may influence the broadening of the plate boundary shear zone (Shillington et al., 2022), so that extensive shallow serpentinization has not occurred in this relatively cold subduction zone. It also implies that accreted terranes in the upper plate (Shillington et al., 2022) are not playing a primary role in the rupture zones of the 2020 and 2021 events, although associated landward increase in rigidity of the upper plate may play some role. For the sections along the Shumagins (Lines 4 and 5), there is an interval of apparent flattening of the interface dip followed by steepening of the interface dip further inland (Fig. 9b and c, respectively). The planar rupture models suggest that slip extends further seaward than the interface steepening. A mild increase in interface dip is also seen for Line 3 and Line 12 (Fig. 9d and e, respectively), indicating a rather gradual dip variation in the Semidi segment along with the change in reflectivity, and it does occur near the up-dip limit of slip in the Chignik event. A much stronger 8–10° increase in the dip of the plate interface offshore of Honshu has been observed at ~12–15 km depth (Ito et al., 2005; Fujie et al., 2006), seaward of the 1994 Sanriku-oki earthquake (Ito et al., 2004). Fujie et al. (2006) noted that the bend occurs near the up-dip limit of some large megathrust earthquakes, but it is notable that the 2011 Tohoku earthquake and the 1896 Meiji earthquake ruptured the shallow region seaward of the bend, with slip in 2011 also extending deeper on the megathrust so it is not clear that the bend strongly controls rupture extent.

An abrupt increase in breadth of the reflecting zone appears to correspond well with the up-dip extent of the 2020 and 2021 ruptures. This likely does not result from thickening of sediments subducted along the megathrust, but suggests different extent of localization of shearing within the underthrust material. This occurs along both the Shumagin and Semidi segments, despite the difference in incoming sediments on the Pacific seafloor, where the thick Zodiak Fan has only intersected the arc along the Semidi segment (von Huene et al., 2012) (Fig. 1a). Subduction of that 600–900 m thick sediment pile appears to result in localization of the shallow megathrust faulting at depths <20 km along the Semidi segment that is not distinctive from the shallow localization observed along the Shumagin segment where a thinner (<300 m) and more irregular sediment section enters the trench (Bécel et al., 2017; Li et al., 2018). Pore-fluid pressure estimates based on P velocity of the sediments suggest that the thicker sediments along the Semidi segment presently support higher pore pressures than the thinner, more intermittent sediments along the Shumagin segment (Li et al., 2018).

Commonly, subduction zone thermal structure is thought to influence the up-dip and down-dip limits of the seismogenic zone through its affects on frictional behavior (Hyndman and Wang, 1993). We used the simple model described earlier to estimate the temperature along the shallow plate interface; a temperature of ~150 °C is near the up-limit of the aftershock activity, located ~80 km landward of the trench at around 18 km depth (Fig. 9). More precise information on depth-dependence of the friction coefficient and coupling of the shallow megathrust is needed to produce a more detailed thermal model. The absence of seismic rupture along the shallow plate boundaries of the Shumagin and Semidi segments may be related to hydration minerals and/or dehydration of stable sliding clays and dissipation of high pore pressures. There is a very limited resolution of coupling at shallow depth along the entire region; the geodetic coupling in both regions can be fully accounted for by localized down-dip strong coupling (Zhao et al., 2022), so the shallow seismogenic potential is very uncertain. In both areas, the plate boundary at shallow depth is quite rough and the complexity of the toe raises the possibility that splay faulting, perhaps involving slow tsunami earthquake occurrence, may compete with megathrust sliding (von Huene et al., 2021; Collot et al., 2004).

Down-dip thickening of the megathrust reflective zone has been observed in other regions, and has been linked to the downdip end of the seismogenic zone (Nedimovic et al., 2003), but for the 2020 and 2021 events, the coseismic rupture is located entirely within the 2–5 km thick band of reflectors. This partly contradicts the interpretation in Li et al. (2015), which suggests that the interface with thin, sharp reflectivity is the primary coupling zone involved in large ruptures in this area and the deeper broader zone may or may not participate in ruptures. Thickening of the reflecting zone below 45 km to 4–5 km may influence the down-dip edge of the rupture, but no abrupt transition such as near 25 km depth is apparent in Fig. 9.

While there is a clear transition in the reflectivity of the megathrust at the up-dip limit of coseismic slip for both the 2020 and 2021 ruptures, it remains challenging to identify the physical controls on the dynamic events. Both events involved strong along-dip transitions from no coseismic slip to large-slip near 25 km depth, and both induced significant Coulomb stress changes on the shallow, localized portion of the megathrust producing relatively little aftershock activity below the continental slope. It is reasonable that the broadening of the reflective zone involves the development of multiple shear zones, possibly with fluid-rich layers, with one or more surfaces being currently active for earthquakes (Li et al., 2015). Thickening by underplating may be enabled by changes in the upper plate rheology near the Moho as well (Shillington et al., 2022). It is plausible that high fluid pressures in the more localized, ~180-m-thick, shallow megathrust shear zone, particularly along the Semidi segment, inhibit velocity weakening behavior, but it is not ruled out that strong locking at shallow depth was simply not close enough to critical failure level to be triggered by the dynamic and static stress perturbations from the deeper large ruptures. If this is the case, there remains potential for future tsunami earthquake failure beneath the continental slope, but more stress build up will be required to overcome the locking.

Historic earthquake activity does not shed much light on this issue. The 1938 aftershock zone shown in Fig. 1a is based on only 10 widely distributed aftershocks (Fig. S10) and should not be taken as a reliable indicator of the large-slip zone in that event, and there is great uncertainty in the depth and lateral extent of earlier events such as the 1788 event along the Semidi segment (Davies et al., 1981). The relatively weak tsunami excitation for the 1938 event suggests that slip in that event was constrained to below the continental shelf, similar to the 2021 event. If this can be confirmed, it will imply that the complex along-dip reflectivity of the plate interface and its associated structural and frictional effects repeatedly influenced the up-dip limit of slip. The possibility of very large-slip, very long recurrence interval tsunami earthquakes along the Semidi and Shumagin regions similar to the 1946 Aleutian earthquake has not been ruled out, although there is no geologic indication of large tsunami earthquakes in these segments. Seafloor geodesy will be required to reliably assess the strain accumulation and any afterslip seaward of the 25-km deep abrupt upper edge of the rupture zone for the 2020 and 2021 earthquakes.

5. Conclusions

In the present study, we determined an improved rupture model of the 2021 M_W 8.2 Chignik, Alaska Peninsula earthquake using an iterative seismic+geodetic finite-fault inversion and tsunami modeling procedure. Tsunami data provide strong constraints on the up-dip extent of rupture due to their excitation over a flat continental shelf, and this allows us to impose constraints on seismo-geodetic inversions that result in a model fitting all of the data. The well-resolved coseismic rupture is confined to 25–40 km depths beneath the continental shelf, with no shallow slip under the continental slope. We propose that the up-dip slip extent appears to be controlled by an along-dip transition in the megathrust shear zone in underthrust sediments, high roughness of the shallow megathrust interface where slip did not penetrate to, and low temperature of the shallow plate boundary. The aftershocks are mainly distributed in the shallow region of the rupture, partly penetrating into the shallow region that did not rupture in the mainshock. However, the

shallow western part of the Semidi segment remains unbroken, and may still be hazardous due to the enhanced CFS promoted by the 2020 Shumagin and 2021 Chignik events, if unstable frictional properties are present. Our findings provide new insights into the physical state of the plate boundary along the eastern Alaska Peninsula subduction zone and help to assess the potential for future tsunamigenic rupture of the shallow portion of the megathrust that did not fail during the large deeper events. Moreover, the 2021 rupture pattern also motivates further efforts to better constrain the rupture extent of the 1938 M_W 8.2 event to evaluate whether the structural controls on the up-dip extent of slip are persistent over multiple earthquake cycles.

CRediT authorship contribution statement

Chengli Liu: Funding acquisition, Investigation, Methodology, Formal analysis, Data curation, Writing – original draft. **Yefei Bai:** Funding acquisition, Investigation, Methodology, Formal analysis, Data curation, Writing – original draft. **Thorne Lay:** Conceptualization, Funding acquisition, Investigation, Formal analysis, Writing – original draft. **Yashan Feng:** Investigation, Methodology, Formal analysis. **Xiong Xiong:** Investigation, Formal analysis.

Declaration of Competing Interest

The authors declare that they have no known competing financial interests or personal relationships that could have appeared to influence the work reported in this paper.

Data availability

The facilities of IRIS Data Services, and specifically the IRIS Data Management Center, were used for access to waveforms, related metadata, and/or derived products used in this study. All teleseismic body wave and regional broadband records can be obtained from the Federation of Digital Seismic Networks (FDSN: https://doi.org/10.7914/SN/IU, https://doi.org/10.7914/SN/II, https://doi.org/10.7914/SN/CN, https://doi.org/10.18715/GEOSCOPE.G, https://doi.org/10.7914/SN/CU, https://doi.org/10.7914/SN/IC, https://doi.org/10.7914/SN/AV, https://doi.org/10.7914/SN/AK, https://doi.org/10.7914/SN/TA), and accessed through the Incorporated Research Institutions for Seismology (IRIS) data management center (http://ds.iris.edu/wilber3/find_stations/11448043). IRIS Data Services are funded through the Seismological Facilities for the Advancement of Geoscience (SAGE) Award of the National Science Foundation under Cooperative Support Agreement EAR-1851048. Recordings from strong-motion sensors can be obtained from the Center for Engineering Strong Motion Data (CESMD, https://www.strongmotioncenter.org/cgi-bin/CESMD/iqr_dist_DM2.pl?IQRID=us6000f02w&SFlag=0&Flag=2). The UNAVCO Bulletin Board provided coseismic GNSS displacements at https://data.unavco.org/archive/gnss/products/event/. Raw GNSS data, primarily from the PBO GPS network used in this study, are available at the GAGE Facility archive, operated by UNAVCO (https://data.unavco.org/archive/gnss/highrate/1-Hz/rinex/2021/210/). The services provided by the GAGE Facility, operated by UNAVCO, Inc., receive support from the National Science Foundation and the National Aeronautics and Space Administration under NSF Cooperative Agreement EAR-1724794. The CSRS-PPP online service system was used for hr-GNSS data processing (https://webapp.geod.nrcan.gc.ca/geod/tools-outils/ppp.php). Earthquake information is based on the catalogs from the U.S. Geological Survey National Earthquake Information Center (USGS-NEIC) (https://earthquake.usgs.gov/earthquakes) and the Alaska Earthquake Center (http://earthquake.alaska.edu), last accessed July 1, 2022. The tide gauge data are provided by the Sea Level Station Monitoring Facility of the Intergovernmental Oceanographic Commission of the United Nations (http://www.ioc-sealevelmonitoring.org/index.php). The DART data can be obtained from the United Sates National Oceanic and Atmospheric Administration (https://www.ndbc.noaa.gov/obs.shtml). The high-resolution digital elevation model, Sand Point V2, at the Shumagin Islands was downloaded from the Nation Centers for Environmental Information (https://maps.ngdc.noaa.gov/viewers/bathymetry/).

Acknowledgments

We thank three anonymous reviewers for their thoughtful comments that helped to improve the presentation. C. Liu was supported by the National Science Foundation of China (No. 42222403, 41974056). Y. Bai's tsunami research is supported by Finance Science and Technology Project of Hainan Province (No. ZDKJ202019). T. Lay's earthquake research is supported by U.S. National Science Foundation (Grant EAR1802364).

Appendix A. Supplementary material

Supplementary data to this article can be found online at https://doi.org/10.1016/j.tecto.2023.229808.

References

Bai, Y., Cheung, K.F., Yamazaki, Y., Lay, T., Ye, L., 2014. Tsunami surges around the Hawaiian Islands from the 1 April 2014 North Chile Mw 8.1 earthquake. Geophys. Res. Lett. 41, 8512–8521. https://doi.org/10.1002/2014GL061686.

Bai, Y., Yamazaki, Y., Cheung, K.F., 2018. Convergence of multilayer nonhydrostatic model in relation to Boussinesq-type equations. J. Waterw. Port Coast. Ocean Eng. 144 (2) https://doi.org/10.1061/(ASCE)WW.1943-5460.0000438, 06018001.

Bai, Y., Liu, C., Lay, T., Cheung, K.F., Ye, L., 2022. Optimizing a model of coseismic rupture for the 22 July 2020 MW 7.8 Simeonof earthquake by exploiting acute sensitivity of tsunami excitation across the shelf break. J. Geophys. Res. Solid Earth 127. https://doi.org/10.1029/2022JB024484 e2022JB024484.

Bécel, A., Shillington, D.J., Delescluse, M., Nedimović, M.R., Abers, G.A., Saffer, D.M., Webb, S.C., Keranen, K.M., Roche, P.-H., Kuehn, H., 2017. Tsunamigenic structures in a creeping section of the Alaska subduction zone. Nat. Geosci. 10 (8), 609–613. https://doi.org/10.1038/ngeo2990.

Cheung, K., Lay, T., Sun, L., Yamazaki, Y., 2022. Tsunami size variability with rupture depth. Nat. Geosci. 15, 33–36. https://doi.org/10.1038/s41561-021-00869-z.

Collot, J.-Y., Marcaillou, B., Sage, F., Michaud, F., Agudelo, W., Charvis, P., Graindorge, D., Gutscher, M.-A., Spence, G., 2004. Are rupture zone limits of great subduction earthquakes controlled by upper plate structures? Evidence from multichannel seismic reflection data acquired across the northern Ecuador—southwest Colombia margin. J. Geophys. Res. 109, B11103. https://doi.org/10.1029/2004JB003060.

Crowell, B.W., Melgar, D., 2020. Slipping the Shumagin gap: a kinematic coseismic and early afterslip model of the Mw 7.8 Simeonof Island, Alaska, earthquake. Geophys. Res. Lett. 47 https://doi.org/10.1029/2020GL090308 e2020GL090308.

Davies, J., Sykes, L., House, L., Jacob, K., 1981. Shumagin seismic gap, Alaska Peninsula: history of great earthquakes, tectonic setting, and evidence for high seismic potential. J. Geophys. Res. 86 (B5), 3821–3855. https://doi.org/10.1029/JB086iB05p03821.

DeMets, C., Gordon, R.G., Argus, D.F., 2010. Geologically current plate motions. Geophys. J. Int. 181, 1–80. https://doi.org/10.1111/j.1365-246X.2009.04491.x.

Drooff, C., Freymueller, J.T., 2021. New constraints on slip deficit on the Aleutian megathrust and inflation at Mt. Veniaminof, Alaska from repeat GPS measurements. Geophys. Res. Lett. 48 (4) https://doi.org/10.1029/2020GL091787 e2020GL091787.

Elliott, J.L., Grapenthin, R., Parameswaran, R.M., Xiao, Z., Freymueller, J.T., Fusso, L., 2022. Cascading rupture of a megathrust. Sci. Adv. 8 (18) https://doi.org/10.1126/sciadv.abm413 eabm4131.

Estabrook, C.H., Jacob, K.H., Sykes, L.R., 1994. Body wave and surface wave analysis of large and great earthquakes along the Eastern Aleutian Arc, 1923-1993: Implications for future events. J. Geophys. Res. 99, 11643–11662. https://doi.org/10.1029/93JB03124.

Fournier, T.J., Freymueller, J.T., 2007. Transition from locked to creeping subduction in the Shumagin region, Alaska. Geophys. Res. Lett. 34 (6) https://doi.org/10.1029/2006GL029073. L06303.

Freed, A.M., 2005. Earthquake triggering by static, dynamic, and postseismic stress transfer. Annu. Rev. Earth Planet. Sci. 33 (1), 335–367. https://doi.org/10.1146/annurev.earth.33.092203.122505.

Freymueller, J.T., Suleimani, E.N., Nicolsky, D.J., 2021. Constraints on the slip distribution of the 1938 MW 8.3 Alaska Peninsula earthquake from tsunami modeling. Geophys. Res. Lett. 48 (9) https://doi.org/10.1029/2021GL092812 e2021GL092812.

Fujie, G., Ito, A., Kodaira, S., Takahashi, N., Kaneda, Y., 2006. Confirming sharp bending of the Pacific plate in the northern Japan trench subduction zone by applying a traveltime mapping method. Phys. Earth Planet. Inter. 157, 72–85.

Fujiwara, T., dos Santos Ferreira, C., Bachmann, A.K., Strasser, M., Weer, G., Sun, T., Kanamatsu, T., Kodaira, S., 2017. Seafloor displacement after the 2011 Tohoku-oki Earthauke in the northern Japan trench examined by repeated bathymetric surveys. Geophys. Res. Lett. 44 https://doi.org/10.1002/2017GL075839, 11,833-11,839.

Hayes, G.P., 2017. The finite, kinematic rupture properties of great-sized earthquakes since 1990. Earth Planet. Sci. Lett. 468, 94–100. https://doi.org/10.1016/j.epsl.2017.04.003.

Hayes, G.P., Moore, G.L., Portner, D.E., Hearne, M., Flamme, H., Furtney, M., Smoczyk, G.M., 2018. Slab2, a comprehensive subduction zone geometry model. Science 362 (6410), 58–61. https://doi.org/10.1126/science.aat4723.

Heidarzadeh, M., Murotani, S., Satake, K., Ishibe, T., Gusman, A.R., 2016. Source model of the 16 September 2015 Illapel, Chile, Mw 8.4 earthquake based on teleseismic and tsunami data. Geophys. Res. Lett. 43, 643–650. https://doi.org/10.1002/2015GL067297.

Hyndman, R.D., Wang, K., 1993. Thermal constraints on the zone of major thrust earthquake failure: the Cascadia subduction zone. J. Geophys. Res. Solid Earth 98 (B2), 2039–2060. https://doi.org/10.1029/92JB02279.

Ichinose, G., Somerville, P., Thio, H.K., Graves, R., O'Connell, D., 2007. Rupture process of the 1964 Prince William Sound, Alaska, earthquake from the combined inversion of seismic, tsunami, and geodetic data. J. Geophys. Res. 112 (B7) https://doi.org/10.1029/2006JB004728. B07306.

Iinuma, T., Hino, R., Kido, M., Inazu, D., Osada, Y., Ito, Y., Ohzono, M., Tsushima, H., Suzuki, S., Fujimoto, H., Miura, S., 2012. Coseismic slip distribution of the 2011 off the Pacific coast of Tohoku Earthquake refined by means of seafloor geodetic data. J. Geophys. Res. Solid Earth 117 (B7). https://doi.org/10.1029/2012JB009186.

Ito, A., Ujie, G., Tsuru, T., Kodaira, S., Nakanishi, A., Kaneda, Y., 2004. Fault plane geometry in the source region of the 1994 Sanriku-oki earthquake. Earth Planet. Sci. Lett. 223, 163–175. https://doi.org/10.1016/j.epsl.2004.04.007.

Ito, A., Fujie, G., Miura, S., Kodaira, S., Kaneda, Y., 2005. Bending of the subducting oceanic plate and its implications for rupture propagation of large interplate earthquakes of Miyagi, Japan, in the Japan Trench subduction zone. Geophys. Res. Lett. 32 https://doi.org/10.1029/2004GL022307. L05310.

Ji, C., Helmberger, D.V., Wald, D.J., Ma, K.F., 2003. Slip history and dynamic implications of the 1999 Chi-Chi, Taiwan, earthquake. J. Geophys. Res. Solid Earth 108 (B9). https://doi.org/10.1029/2002JB001764.

Johnson, J.M., Satake, K., 1994. Rupture extent of the 1938 Alaskan earthquake as inferred from tsunami waveforms. Geophys. Res. Lett. 21, 733–736. https://doi.org/10.1029/94GL00333.

Johnson, J.M., Satake, K., 1997. Estimation of seismic moment and slip distribution of the April 1, 1946, Aleutian tsunami earthquake. J. Geophys. Res. 102 (B6), 11765–11774. https://doi.org/10.1029/97JB00274.

Kido, M., Osada, Y., Fujimoto, H., Hino, R., Ito, Y., 2011. Trench-normal variation in observed seafloor displacements associated with the 2011 Tohoku-oki earthquake. Geophys. Res. Lett. 38 https://doi.org/10.1029/2011GL050057. L24303.

Kuehn, H., 2019. Along-Trench Segmentation and Down-Dip Limit of the Seismogenic Zone at the Eastern Alaska-Aleutian Subduction Zone. Ph.D. Thesis,. Dalhousie University, 334 pp. http://hdl.handle.net/10222/75145.

Lay, T., 2018. A review of rupture characteristics of the 2011 Tohoku-oki MW 9.1 earthquake. Tectonophys. 7833, 4–36. https://doi.org/10.1016/j.tecto.2017.09.022.

Lay, T., Kanamori, H., Ammon, C.J., Koper, K.D., Hutko, A.R., Ye, L., Yue, H., Rushing, T. M., 2012. Depth-varying rupture properties of subduction zone megathrust faults. J. Geophys. Res. Solid Earth 117 (B4). https://doi.org/10.1029/2011JB009133. B04311.

Lay, T., Liu, C., Kanamori, H., 2019. Enhancing tsunami warning using P wave coda. J. Geophys. Res. Solid Earth 124. https://doi.org/10.1029/2019JB018221, 10,583-10,609.

Li, L., Cheung, K.F., 2019. Numerical dispersion in non-hydrostatic modeling of long-wave propagation. Ocean Model 138, 68–87. https://doi.org/10.1016/j.ocemod.2019.05.002.

Li, S., Freymueller, J.T., 2018. Spatial variation of slip behavior beneath the Alaska Peninsula along Alaska-Aleutian subduction zone. Geophys. Res. Lett. 45 (8), 3453–3460. https://doi.org/10.1002/2017GL076761.

Li, J., Shillington, D.J., Becél, A., Nedimovic, M.R., Webb, S.C., Saer, D.M., et al., 2015. Downdip variations in seismic reflection character. Implications for fault structure and seismogenic behavior in the Alaska subduction zone. J. Geophys. Res. Solid Earth 120, 7883–7904. https://doi.org/10.1002/2015JB012338.

Li, J., Shillington, D.J., Safer, D.M., Bécel, A., Nedimovic, M.R., Kuehn, H., Webb, S.C., Keranen, K.M., Abers, G.A., 2018. Connections between subducted sediment, pore-fluid pressure and earthquake behavior along the Alaska megathrust. Geology 46, 299–302. https://doi.org/10.1130/G39557.1.

Liu, C., Lay, T., Xiong, X., Wen, Y., 2020. Rupture of the 2020 Mw 7.8 earthquake in the Shumagin gap inferred from seismic and geodetic observations. Geophys. Res. Lett. 47 (22) https://doi.org/10.1029/2020GL090806 e2020GL090806.

Liu, C., Lay, T., Xiong, X., 2022. The 29 July 2021 Mw 8.2 Chignik, Alaska Peninsula earthquake rupture inferred from seismic and geodetic observations: Re-rupture of the western 2/3 of the 1938 rupture zone. Geophys. Res. Lett. 49 (4) https://doi.org/10.1029/2021GL096004 e2021GL096004.

Maksymowicz, A., Chadwell, D.D., Ruiz, J., Tréhu, A.M., Contreras-Reyes, E., Weinrebe, W., Diaz-Naveas, J., Gibson, J.C., Lonsdale, P., Tryon, M.D., 2017. Coseismic seafloor deformation in the trench region during the Mw8.8 Maule megathrust earthquake. Sci. Rep. 7, 45918. https://doi.org/10.1038/srep45918.

Molnar, P., England, P., 1990. Temperatures, heat flux, and frictional stress near major thrust faults. J. Geophys. Res. Solid Earth 95 (B4), 4833–4856. https://doi.org/10.1029/JB095iB04p04833.

Mulia, I.E., Heidarzadeh, M., Satake, K., 2022a. Effects of depth of fault slip and continental shelf geometry on the generation of anomalously long-period tsunami by the July 2020 M_W 7.8 Shumagin (Alaska) earthquake. Geophys. Res. Lett. 49 https://doi.org/10.1029/2021GL094937 e2021GL094937.

Mulia, I.E., Gusman, A.R., Heidarzadeh, M., Satake, K., 2022b. Sensitivity of tsunami data to the up-dip extent of the July 2021 Mw 8.2 Alaska Earthquake. Seismol. Res. Lett. 93, 1992–2003. https://doi.org/10.1785/0220210359.

Nedimovic, M.R., Hyndman, R.D., Ramachandran, K., Spence, G.D., 2003. Reflection signature of seismic and aseismic slip on the northern Cascadia subduction interface. Nature 424, 416–420. https://doi.org/10.1038/nature01840.

Niazi, M., Chun, K.Y., 1989. Crustal structure in the southern Bering shelf and the Alaska peninsula from inversion of surface-wave dispersion data. Bull. Seismol. Soc. Am. 79 (6), 1883–1893. https://doi.org/10.1785/BSSA0790061883.

Okada, Y., 1985. Surface deformation due to shear and tensile faults in a half space. Bull. Seismol. Soc. Am. 75 (4), 1135–1154. https://doi.org/10.1785/BSSA0750041135.

Ripperger, J., Mai, P.M., 2004. Fast computation of static stress changes on 2D faults from final slip distributions. Geophys. Res. Lett. 31 (18) https://doi.org/10.1029/2004GL020594. L18610.

Romano, F., Lorito, S., Lay, T., Piatanesi, A., Volpe, M., Murphy, S., Tonini, R., 2020. Benchmarking the Optimal Time Alignment (OTA) of tsunami waveforms in nonlinear joint inversions for the MW 8.8 2010 Maule (Chile) earthquake. Front. Earth Sci. 8, 585429 https://doi.org/10.3389/feart.2020.585429.

Sallarés, V., Ranero, C.R., 2019. Upper-plate rigidity determines depth-varying rupture behavior of megathrust earthquakes. Nature 576, 96–101. https://doi.org/10.1038/s41586-019-1784-0.

Sato, M., Ishikawa, T., Ujihara, N., Yoshida, S., Fujita, M., Mochizuki, M., Asada, A., 2011. Displacement above the hypocenter of the 2011 Tohoku-oki earthquake. Science 332, 1395. https://doi.org/10.1126/science.1207401.

Scholz, C.H., 2019. The Mechanics of Earthquakes and Faulting, 3rd edn. Cambridge Univ. Press.

Shao, G., Li, X., Ji, C., Maeda, T., 2011. Focal mechanism and slip history of the 2011 Mw 9.1 off the Pacific coast of Tohoku Earthquake, constrained with teleseismic body and surface waves. Earth Planets Space 63 (7), 559–564. https://doi.org/10.5047/eps.2011.06.028.

Shillington, D.J., Bécel, A., Nedimovic, M.R., 2022. Upper plate structure and megathrust properties in the Shumagin gap near the July 2020 M7.8 Simeonof event. Geophys. Res. Lett. 49 https://doi.org/10.1029/2021GL096974, 32021GL096974.

Sykes, L.R., 1971. Aftershock zones of great earthquakes, seismicity gaps, and earthquake prediction for Alaska and the Aleutians. J. Geophys. Res. 76 (32), 8021–8041. https://doi.org/10.1029/JB076i032p08021.

Tanioka, Y., Satake, K., 1995. Tsunami generation by horizontal displacement of ocean bottom. Geophys. Res. Lett. 23 (88), 861–864. https://doi.org/10.1029/96GL00736.

Tanioka, Y., Seno, T., 2001. Detailed analysis of tsunami waveforms generated by the 1946 Aleutian tsunami earthquake. Nat. Hazards Earth Syst. Sci. 1 (4), 171–175. https://doi.org/10.5194/nhess-1-171-2001.

Tomito, F., Kido, M., Ohta, Y., Iinuma, T., Hino, R., 2017. Along-trench variation in seafloor displacements after the 2011 Tohoku earthquake. Sci. Adv. 3 https://doi.org/10.1126/sciadv.1700113 e1700133.

United States Geological Survey National Earthquake Information Center, 2021. M 8.2–99 km S.E. of Perryville, Alaska. https://earthquake.usgs.gov/earthquakes/eventpage/ak0219neiszm/finite-fault.

von Huene, R., Miller, J.J., Weinrebe, W., 2012. Subducting plate geology in three great earthquake ruptures of the western Alaska margin, Kodiak to Unimak. Geosphere 8, 628–644. https://doi.org/10.1130/GES00715.1.

von Huene, R., Miller, J.J., Krabbenhoeft, A., 2021. The Alaska convergent margin backstop splay fault zone, a potential large tsunami generator between the frontal prism and continental framework. Geochem. Geophys. Geosyst. 22 https://doi.org/10.1029/2019GC008901 e2019GC008901.

Wirp, S.A., Gabriel, A.-A., Schmeller, M., Madden, E.H., van Zelst, I., Krenz, L., van Dinther, Y., Rannabauer, L., 2021. 3D linked subduction, dynamic rupture, tsunami, and inundation modeling: Dynamic effects of supershear and tsunami earthquakes, hypocenter location, and shallow fault slip. Front. Earth Sci. 9 https://doi.org/10.3389/feart.2021.626844, 626844.

Xiao, Z., Freymueller, J.T., Grapenthin, R., Elliott, J.L., Drooff, C., Fusso, L., 2021. The deep Shumagin gap filled: Kinematic rupture model and slip budget analysis of the 2020 Mw 7.8 Simeonof earthquake constrained by GNSS, global seismic waveforms, and floating InSAR. Earth Planet. Sci. Lett. 576, 117241 https://doi.org/10.1016/j.epsl.2021.117241.

Yamazaki, Y., Lay, T., Cheung, K.F., Yue, H., Kanamori, H., 2011. Modeling near-field tsunami observations to improve finite-fault slip models for the 11 March 2011 Tohoku earthquake. Geophys. Res. Lett. 38 (7) https://doi.org/10.1029/2011GL049130. L00G15.

Yamazaki, Y., Cheung, K.F., Lay, T., 2017. A self-consistent fault slip model or the 2011 Tohoku earthquake and tsunami. J. Geophys. Res. Solid Earth 123, 1435–1458. https://doi.org/10.1002/2017JB014749.

Ye, L., Lay, T., Kanamori, H., Rivera, L., 2016. Rupture characteristics of major and great (Mw≥7.0) megathrust earthquakes from 1990 to 2015: 1. Source parameter scaling relationships. J. Geophys. Res. Solid Earth 121 (2), 826–844. https://doi.org/10.1002/2015JB012426.

Ye, L., Kanamori, H., Lay, T., 2018. Global variations of large megathrust earthquake rupture characteristics. Sci. Adv. 4 https://doi.org/10.1126/sciadv.aao4915 eaao4915.

Ye, L., Lay, T., Kanamori, H., Yamazaki, Y., Cheung, K.F., 2021. The 22 July 2020 Mw 7.8 Shumagin seismic gap earthquake: Partial rupture of a weakly coupled megathrust. Earth Planet. Sci. Lett. 562 https://doi.org/10.1016/j.epsl.2021.116879, 116879.

Ye, L., Bai, Y., Si, D., Lay, T., Cheung, K.F., Kanamori, H., 2022. Rupture model for the 29 July 2021 Mw 8.2 Chignik, Alaska earthquake constrained by seismic, geodetic, and tsunami observations. J. Geophys. Res. Solid Earth 127. https://doi.org/10.1029/2021JB023676 e2021JB023676.

Yin, J., Denolle, M.A., 2021. The Earth's surface controls the depth-dependent seismic radiation of megathrust earthquakes. AGU Adv. 2 https://doi.org/10.1029/2021AV000413 e2021AV000413.

Yue, H., Lay, T., Rivera, L., An, C., Vigny, C., Tong, X., Báez Soto, J.C., 2014. Localized fault slip to the trench in the 2010 Maule, Chile Mw=8.8 earthquake from joint inversion of high-rate GPS, teleseismic body waves, InSAR, campaign GPS, and tsunami observations. J. Geophys. Res. Solid Earth 119, 7786–7804. https://doi.org/10.1002/2014JB011340.

Zhao, B., Bürgmann, R., Wang, D., Zhang, J., Yu, J., Li, Q., 2022. Aseismic slip and recent ruptures of persistent asperities along the Alaska-Aleutian subduction zone. Nat. Commun. https://doi.org/10.1038/s41467-022-30883-7.

Supplementary Materials for

Megathrust complexity delimited the up-dip extent of slip during the 2021 Chignik, Alaska Peninsula earthquake

Chengli Liu[a*], Yefei Bai[b,c*], Thorne Lay[d], Yashan Feng[a], Xiong Xiong[a]

[a] School of Geophysics and Geomatics, China University of Geosciences, Wuhan, Hubei, 430074, China

[b] Ocean College, Zhejiang University, Zhoushan, Zhejiang, 316021, China.

[c] Hainan Institute, Zhejiang University, Sanya, Hainan, 572024, China.

[d] Department of Earth and Planetary Sciences, University of California Santa Cruz, Santa Cruz, CA, 95064, USA.

*Corresponding authors: Chengli Liu and Yefei Bai

Email: liuchengli@cug.edu.cn; yfbai@zju.edu.cn

This file includes nine Figures and one Table.

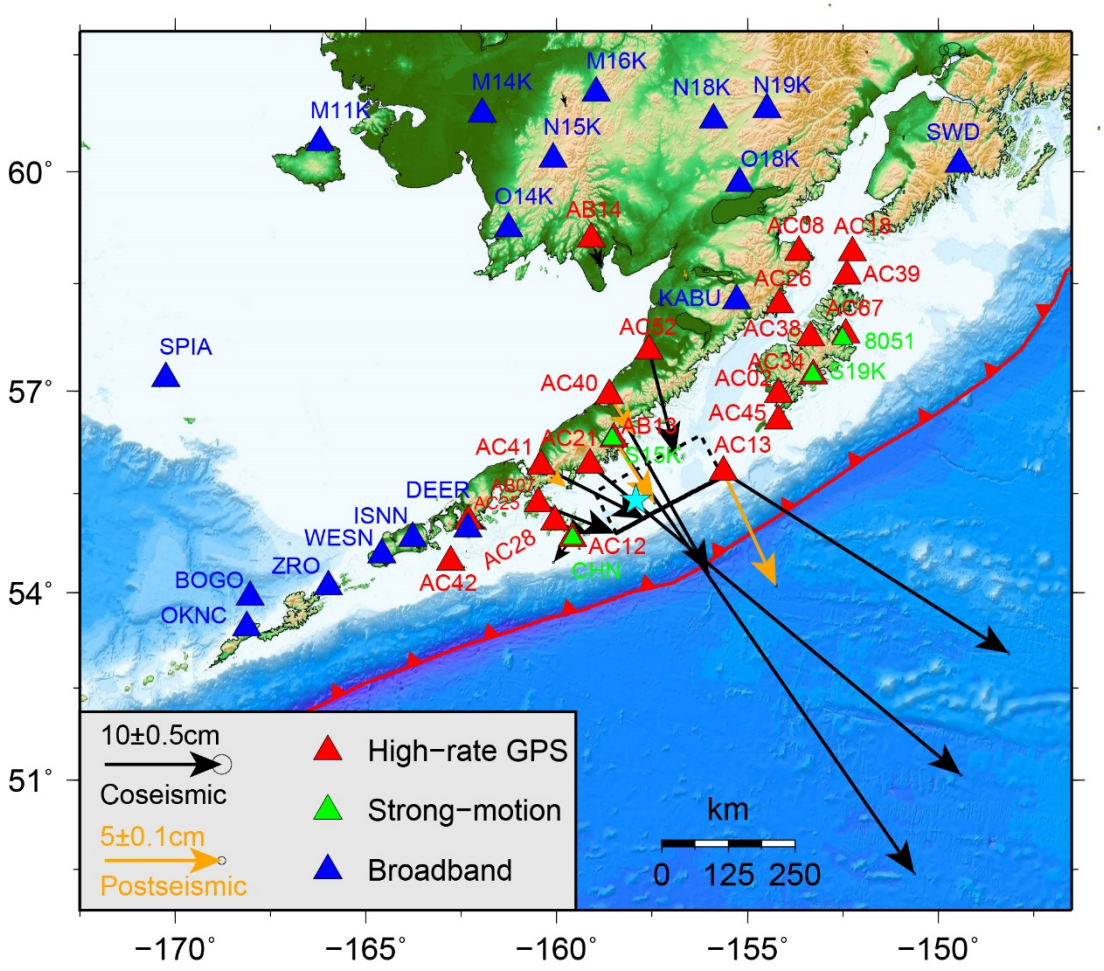

Fig. S1 Distribution of the regional broadband, strong-motion, and high-rate GNSS stations providing data for the joint inversion. Black vectors indicate observed horizontal static GNSS displacements, and orange vectors show the 10 days postseismic slip. The mainshock epicenter is shown by the cyan star, and the black rectangle represents the fault model margins, with a solid line showing the shallow edge. The red barbed line shows the plate boundary between the Pacific plate and the North American plate.

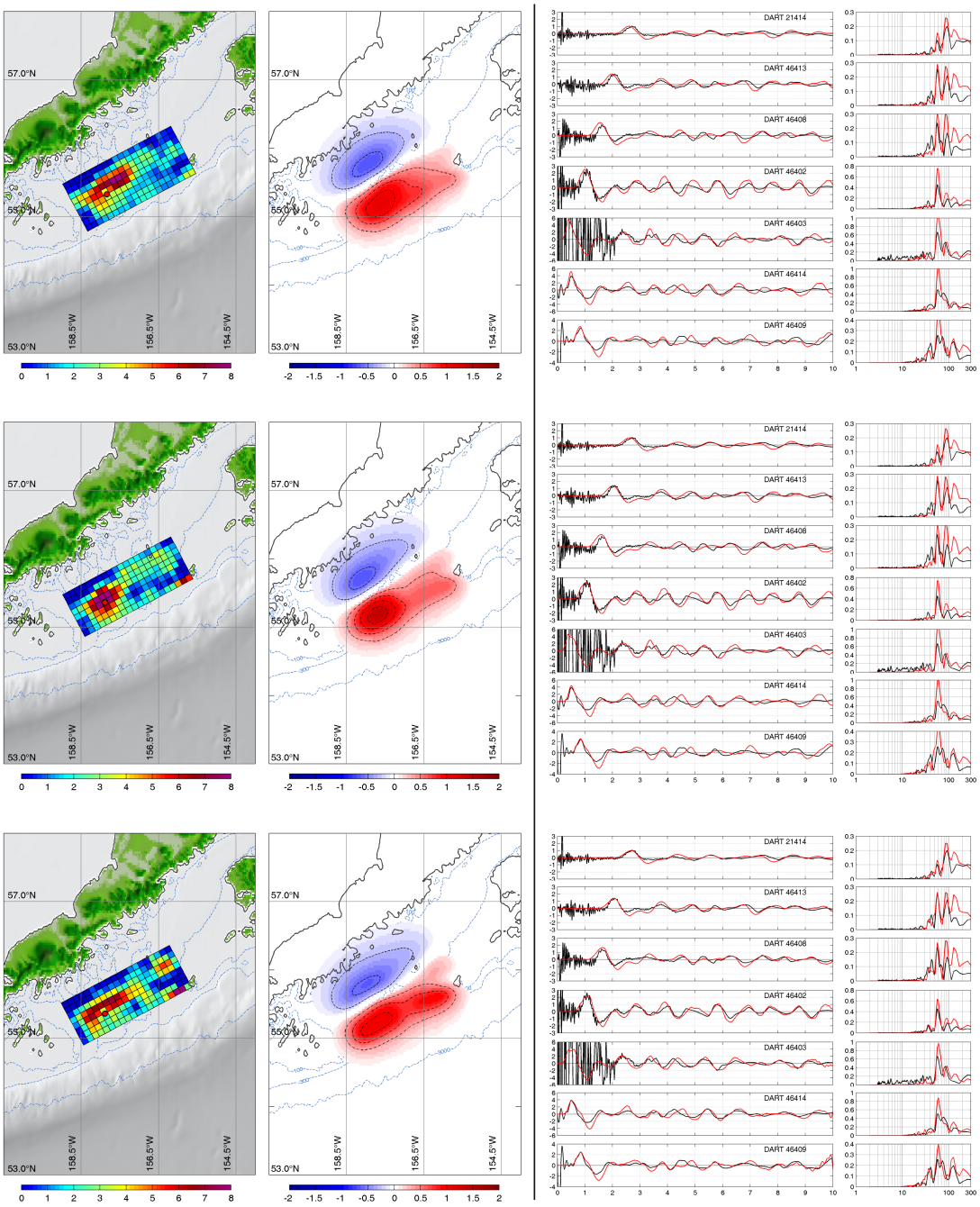

21

22 **Fig. S2 Sensitivity tests of the tsunami arrivals at DART stations to the seaward extent of the**
23 **model grids. The left two columns show the slip models for different up-dip grids and modeled**
24 **seafloor deformation. The right two columns show the corresponding tsunami predictions,**
25 **indicating that the tsunami first arrivals at most stations are sensitive to the up-dip extent of**
26 **the rupture.**

27

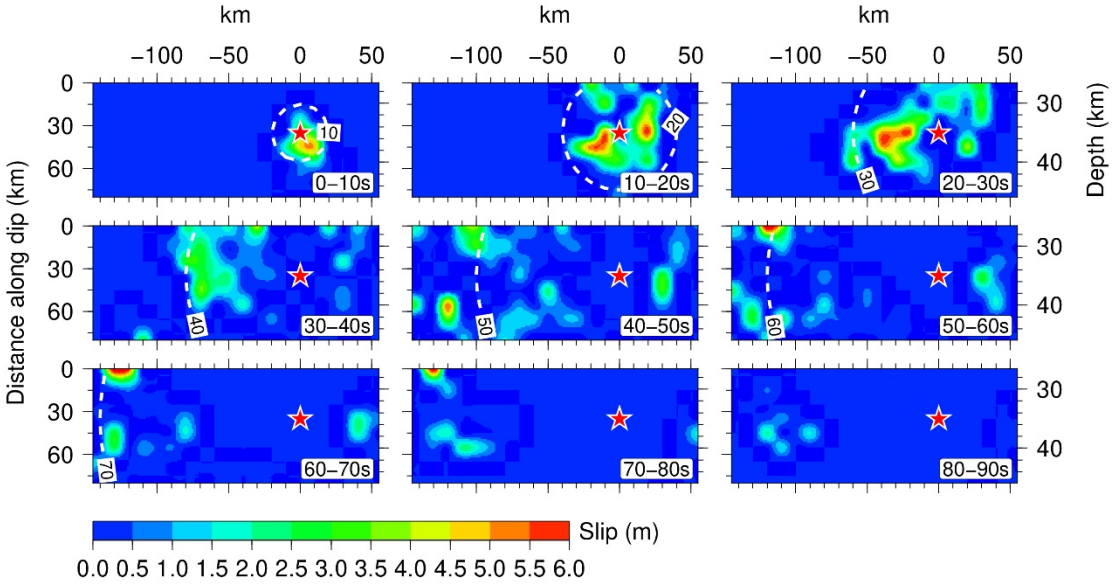

Fig. S3 Snapshots of the rupture history of the final model for the 29 July 2021 M_W 8.2 Chignik with a time interval of 10 s. The white dashed contour denotes the position of a reference rupture front with a rupture velocity of 2.0 km/s, and colors indicate the slip magnitude. The minor slip after 90 s and slip less than 0.5 m anywhere are not considered well-resolved and are truncated correspondingly.

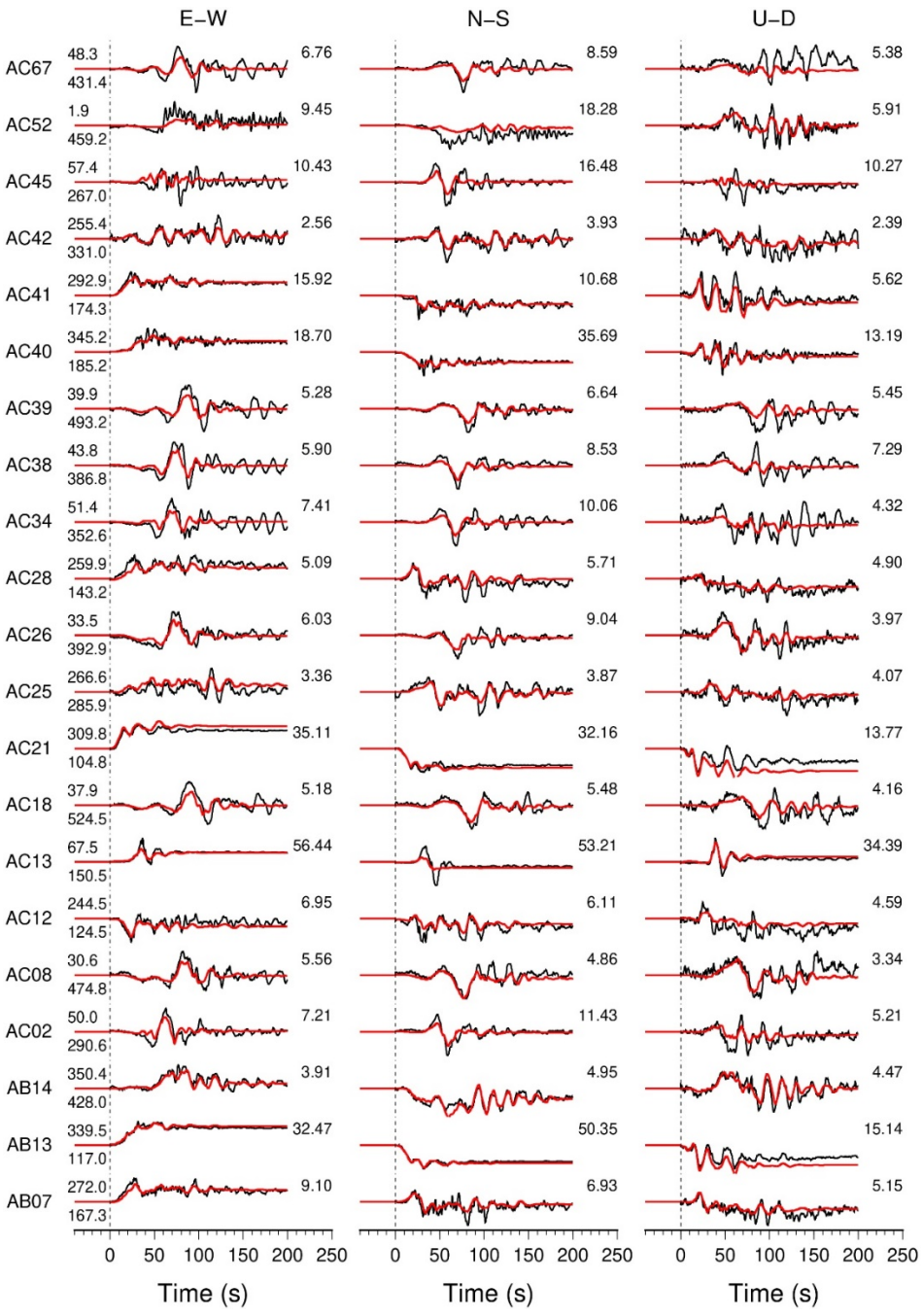

Fig. S4 Comparisons of all high-rate GNSS displacement time series (black) and synthetic seismograms (red) for the final mainshock slip model in Fig. 5a. Data and synthetics are aligned on the first *P* arrivals. The station name is listed on the left of each row; the numbers at the upper right of each waveform comparison indicate the peak observed displacements in cm. The azimuth (above) in degrees and epicentral distance (below) in km are shown at the beginning of each record.

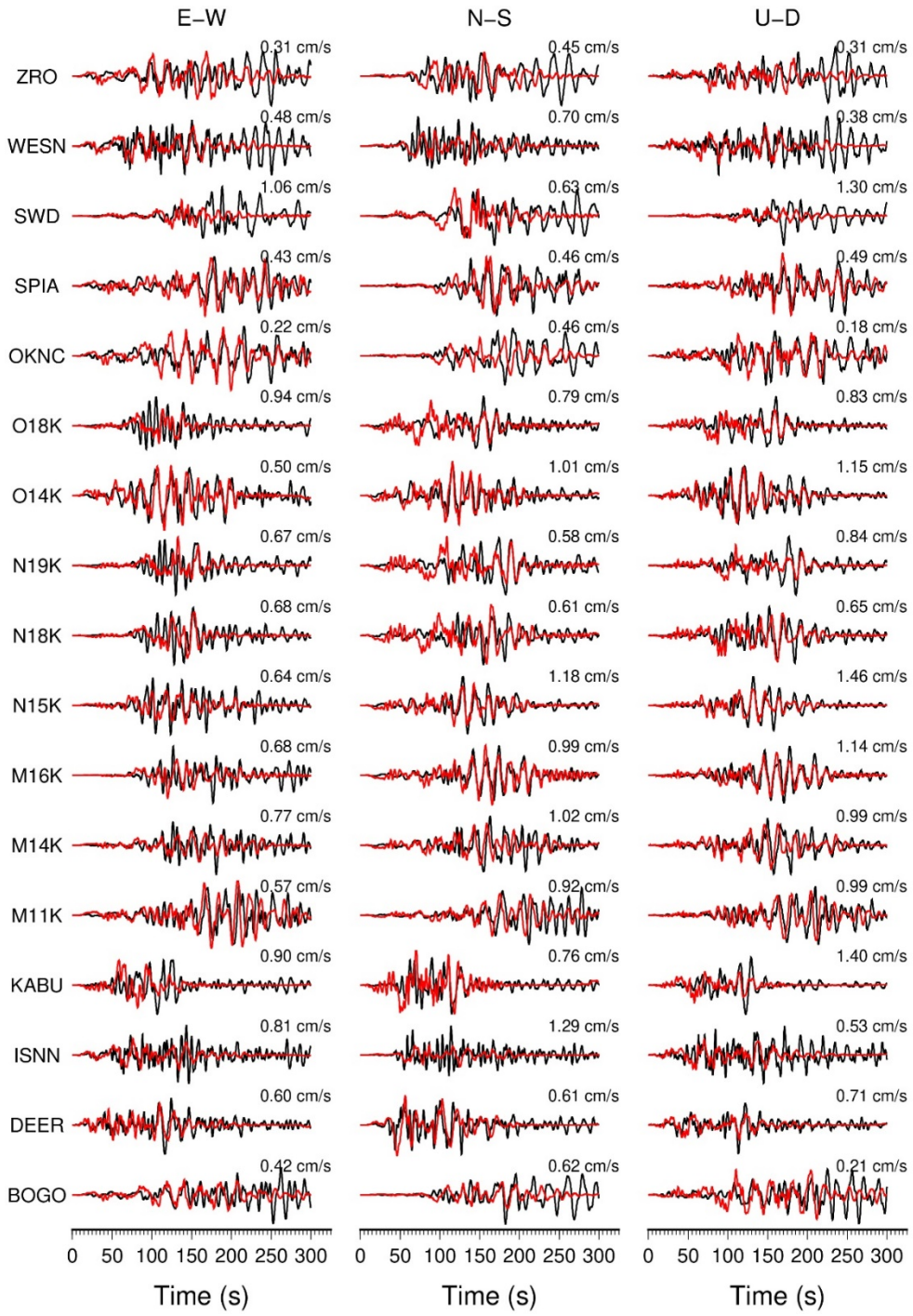

Fig. S5 Comparisons of all regional three-component broadband ground velocity observations (black) and synthetic seismograms (red) for the final mainshock slip model in Fig. 5a. Data and synthetics are aligned on the first *P* arrivals. The station name is listed on the left of each row; the numbers at the upper right of each waveform comparison indicate the maximum observed ground velocity in cm/s.

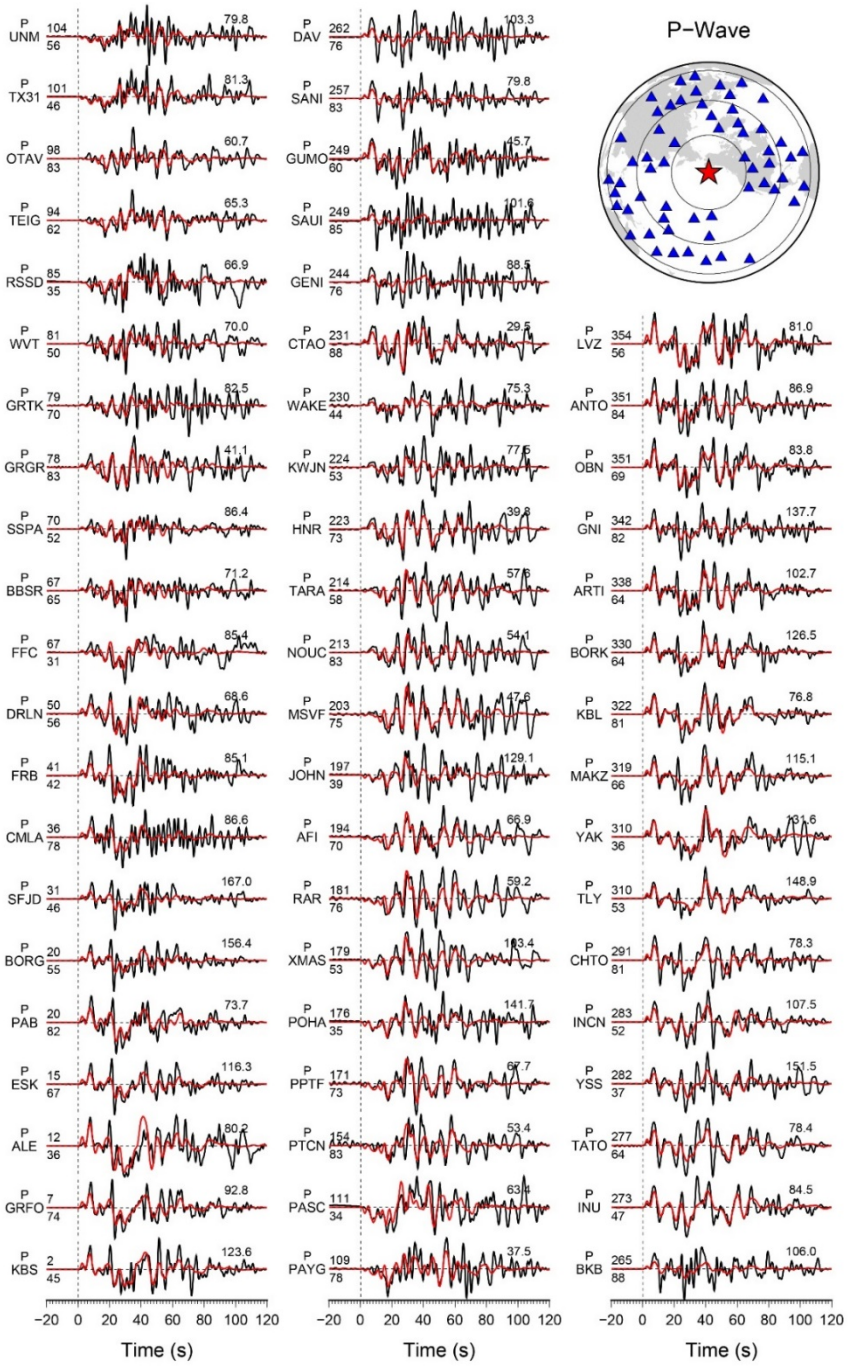

Fig. S6 Comparison of observed (black) and synthetic (red) teleseismic *P* wave ground velocities for the final mainshock slip model shown in Fig. 5a. Data and synthetic seismograms are manually aligned on the first arrivals. Station names and phase-type are indicated on the left of each comparison. The azimuth (above) and epicentral distance (below) in degrees are shown at the beginning of each record. The number above the right portion of each comparison is the peak amplitude of the observed ground velocity in μm/s. The inset in the upper right corner shows the station distribution.

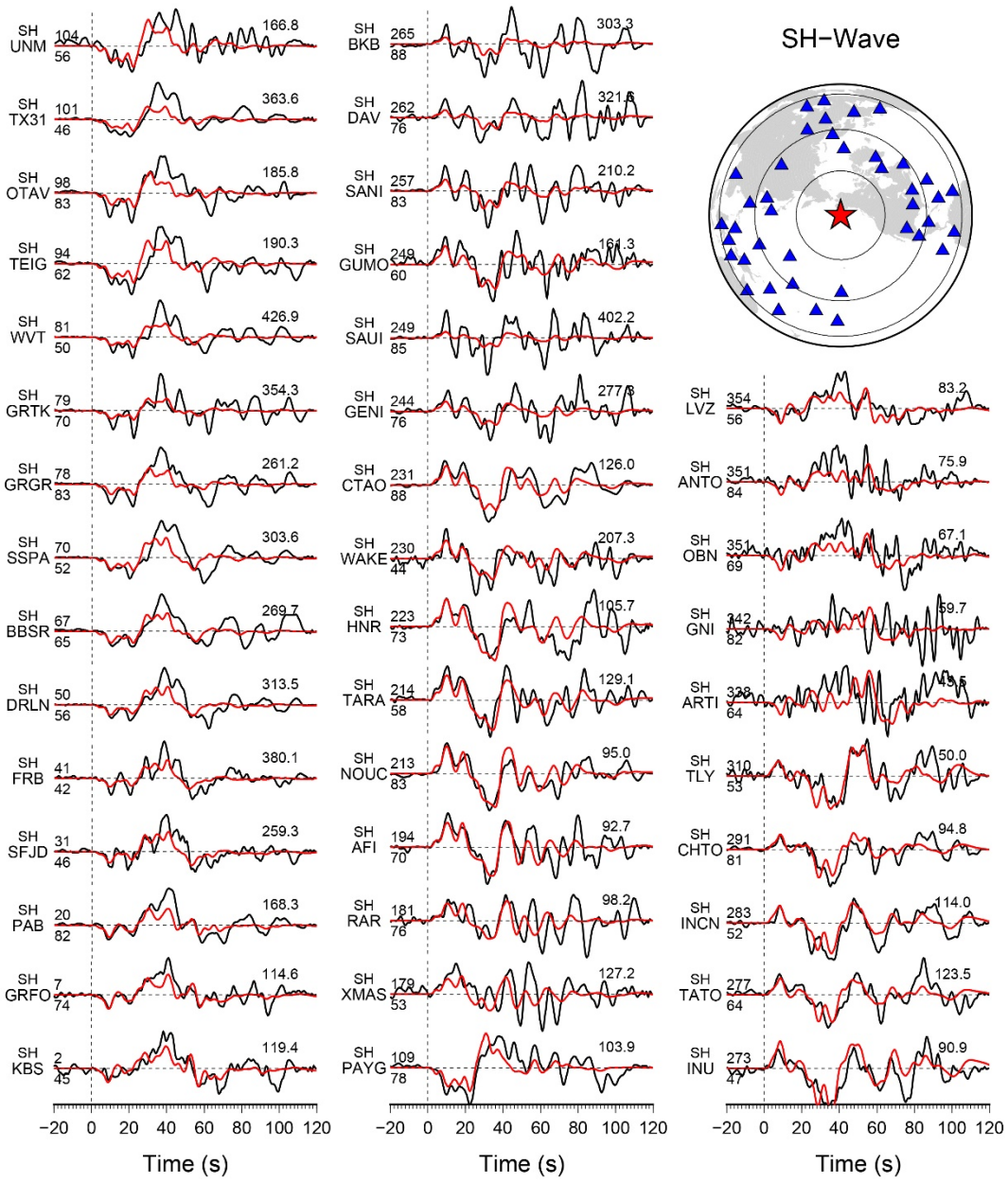

Fig. S6 Continued, but for *SH*-waves.

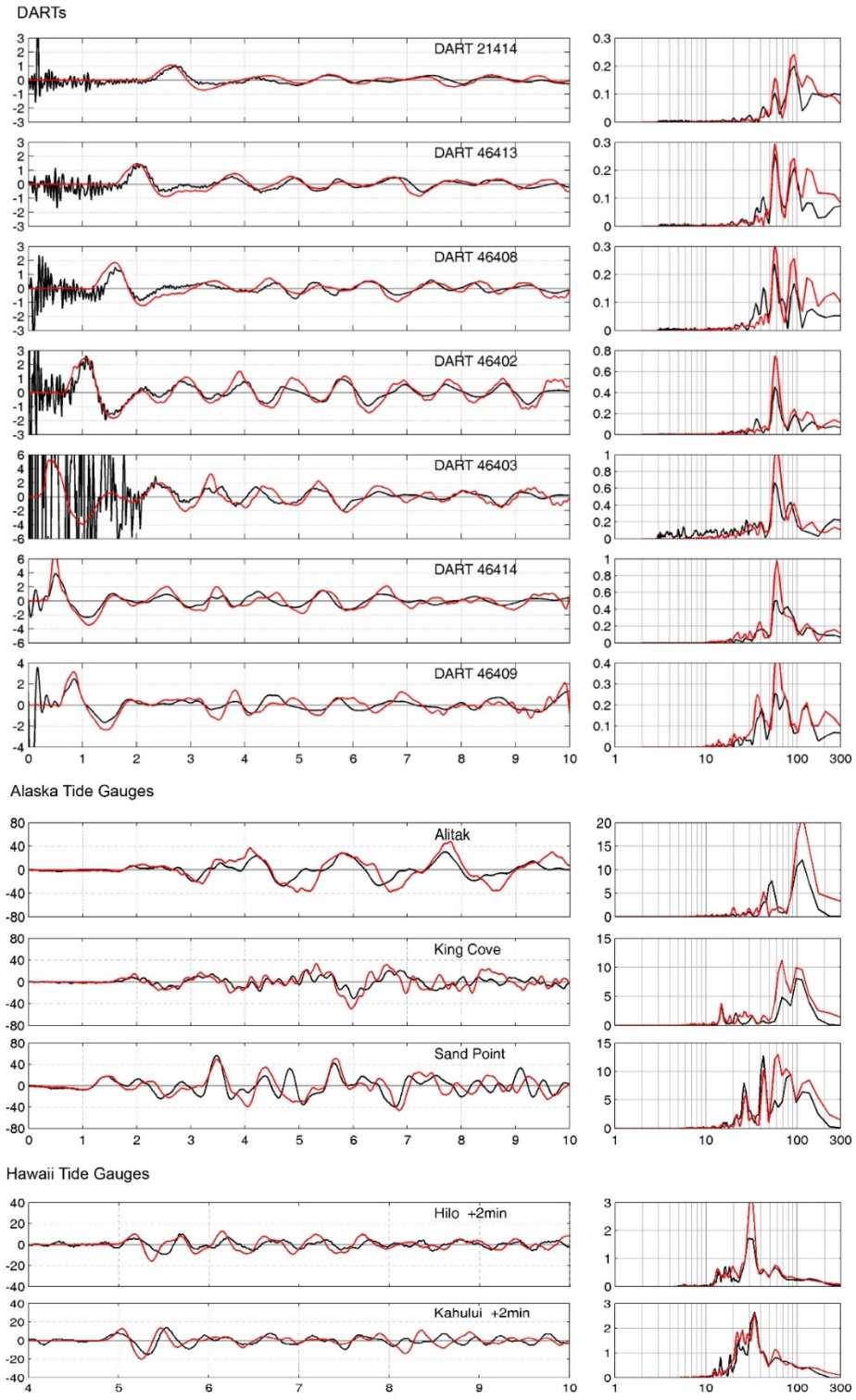

Fig. S7 Tsunami predictions at DARTs and Tide Gauges for the finite-fault slip model of Elliott et al. (2022). Observed tsunami waves are shown in black, and predicted tsunami signals are shown in red.

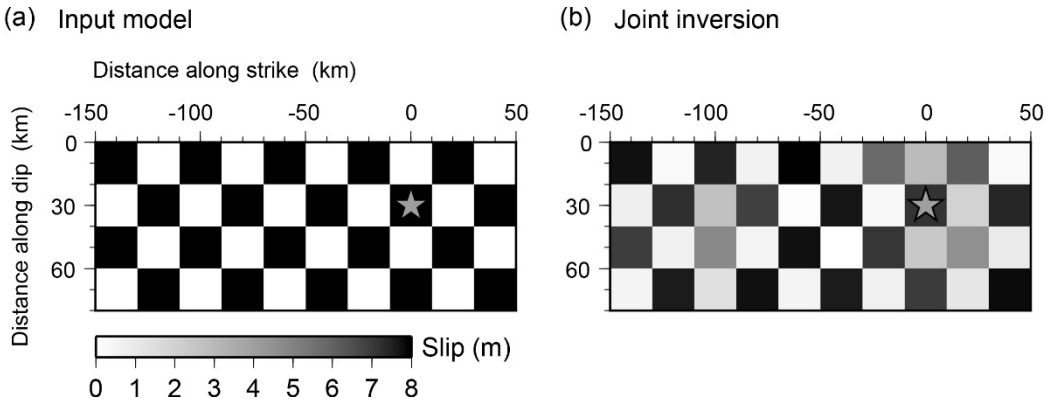

Fig. S8 Resolution test of the joint inversion. (a) Input model with 20 × 20 km subfault patches with a bimodal slip of zero and 8 m. Synthetic observations are computed for this slip model at all actual data positions. (b) The corresponding inversion slip model from a joint inversion of the synthetic observations.

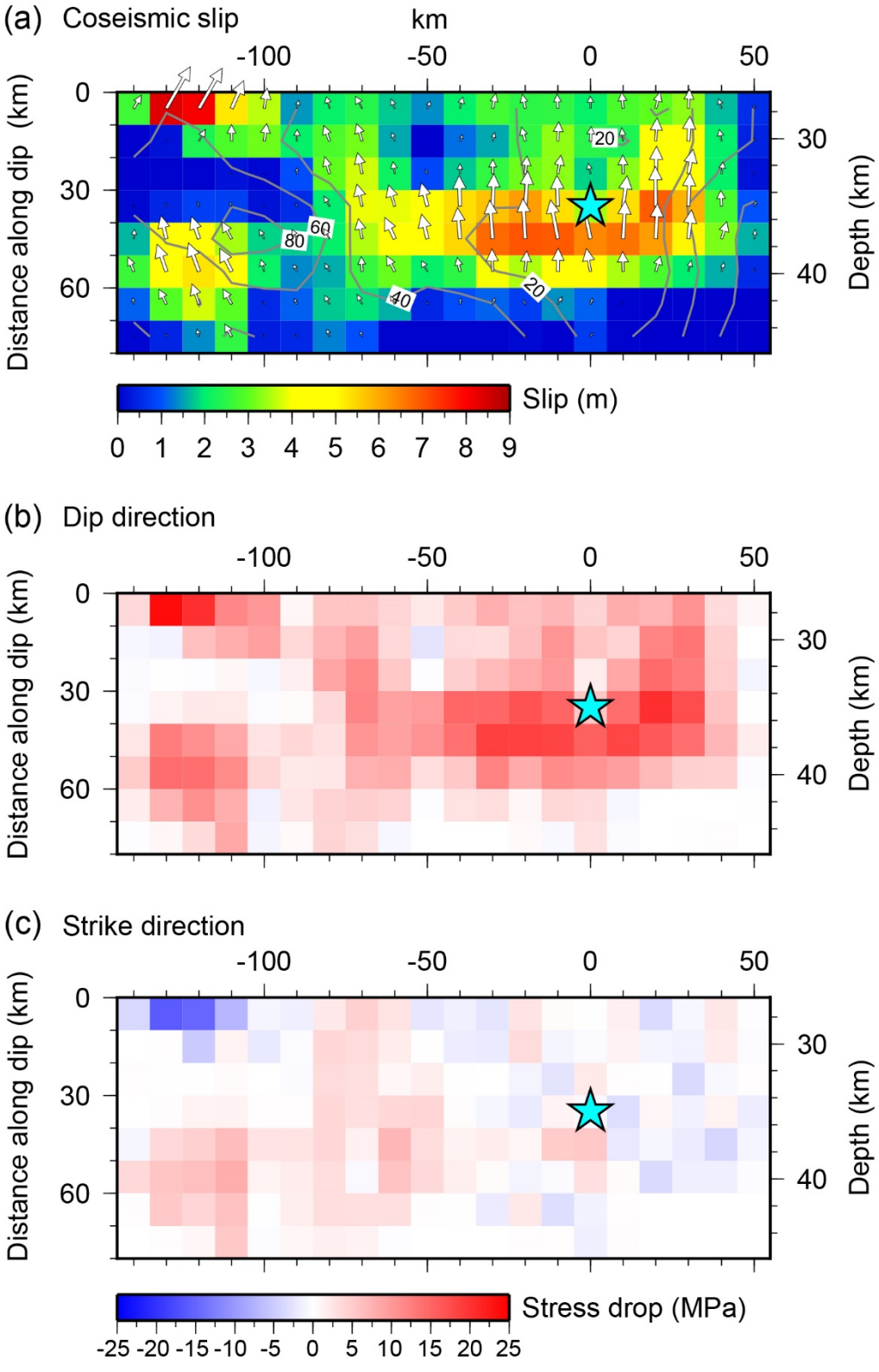

Fig. S9 Final slip model of the 2021 M_W 8.2 Chignik earthquake (a), and corresponding computed static stress drop for the components of slip along the dip direction (b) and along the strike direction (c).

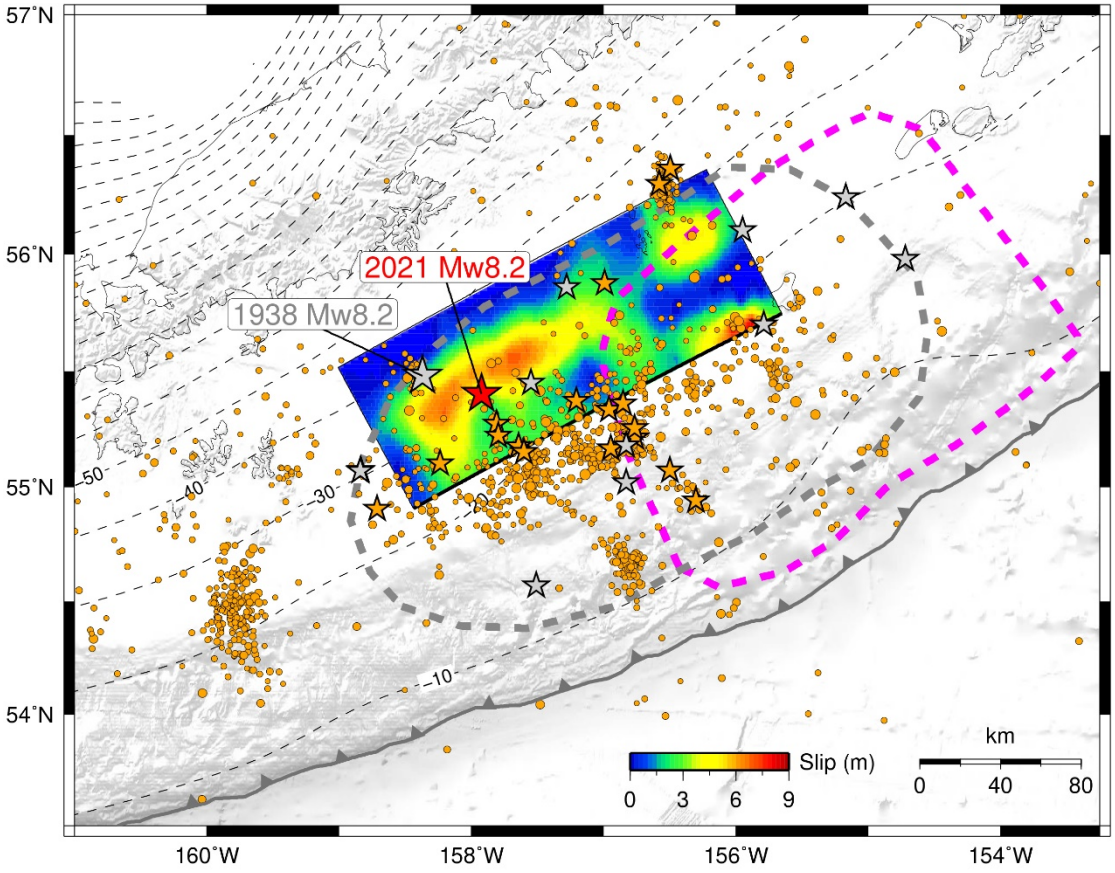

Fig. S10 Comparison of the aftershock zones between the 1938 event and 2021 event. Gray stars represent the 10 widely distributed aftershocks that defined the extent of the 1938 rupture zone (gray dashed line). The orange dots and stars indicate the aftershocks distribution of the 2021 event. The thick magenta dashed line outlines the tsunami source model determined by Freymueller et al. (2021).

79 **Table S1. Parameter values used in the thermal model calculations.**

Parameter	Meaning	Value
K_m	Thermal conductivity in the mantle	3.3 $W \cdot m^{-1} \cdot K^{-1}$
K_s	Thermal conductivity in the wedge	2.55 $W \cdot m^{-1} \cdot K^{-1}$
T_0	Temperature at the base of the lithosphere	1350 ˚C
t_0	Age of subducting oceanic crust at the trench	52 Ma
A_r	Average radiogenic heat production in the upper plate	10^{-6} $W \cdot m^{-3}$
b	Geometric constant	1.0
V	Long-term average fault slip rate	60 $mm \cdot yr^{-1}$
δ	Average dip of subduction thrust interface	10˚
λ	Pore fluid factor	0.95
ρ	Average density of the rocks overlying the plate interface	2700 $kg \cdot m^{-3}$
μ	Frictional coefficient	0.6
κ	Thermal diffusivity	10^{-6}

80